

# The Mass and Momentum Outflow Rates of Photoionized Galactic Outflows

John Chisholm<sup>1</sup>\*, Christy A. Tremonti<sup>2</sup>, Claus Leitherer<sup>3</sup>, Yanmei Chen<sup>4</sup>

<sup>1</sup> *Observatoire de Genève, Université de Genève, 51 Ch. des Maillettes, 1290 Versoix, Switzerland*

<sup>2</sup> *Astronomy Department, University of Wisconsin, Madison, 475 N. Charter St., WI 53711, USA*

<sup>3</sup> *Space Telescope Science Institute, 3700 San Martin Drive, Baltimore, MD 21218, USA*

<sup>4</sup> *Department of Astronomy, Nanjing University, Nanjing 210093, China*

10 May 2017

## ABSTRACT

Galactic outflows are believed to play an important role in regulating star formation in galaxies, but estimates of the outflowing mass and momentum have historically been based on uncertain assumptions. Here, we measure the mass, momentum, and energy outflow rates of seven nearby star-forming galaxies using ultraviolet absorption lines and observationally motivated estimates for the density, metallicity, and radius of the outflow. Low-mass galaxies generate outflows faster than their escape velocities with mass outflow rates up to twenty times larger than their star formation rates. These outflows from low-mass galaxies also have momenta larger than provided from supernovae alone, indicating that multiple momentum sources drive these outflows. Only 1-20% of the supernovae energy is converted into kinetic energy, and this fraction decreases with increasing stellar mass such that low-mass galaxies drive more efficient outflows. We find scaling relations between the outflows and the stellar mass of their host galaxies ( $M_*$ ) at the 2-3 $\sigma$  significance level. The mass-loading factor, or the mass outflow rate divided by the star formation rate, scales as  $M_*^{-0.4}$  and with the circular velocity as  $v_{\text{circ}}^{-1.6}$ . The scaling of the mass-loading factor is similar to recent simulations, but the observations are a factor of five smaller, possibly indicating that there is a substantial amount of unprobed gas in a different ionization phase. The outflow momenta are consistent with a model where star formation drives the outflow while gravity counteracts this acceleration.

**Key words:** ISM: jets and outflows, galaxies: evolution, galaxies: formation, ultraviolet: ISM

## 1 INTRODUCTION

In actively star forming galaxies, high-mass stars inject energy and momentum into the surrounding gas, heating and accelerating the gas out of star-forming regions as a galactic outflow (Heckman et al. 2000; Veilleux et al. 2005; Erb 2015). Models suggest that removing this residual mass and energy from star-forming regions regulates star formation in galaxies (Dekel & Silk 1986; White & Frenk 1991; Katz et al. 1996; Hopkins et al. 2014). Consequently, galactic outflows are a ubiquitous component of modern galaxy formation and evolution simulations (Springel & Hernquist 2003; Hopkins et al. 2014; Vogelsberger et al. 2014; Schaye et al. 2015). However, it is computationally infeasible, at the moment, to fully resolve all of the necessary physics to drive galactic outflows, and simulations typically scale the mass and energy outflow rates with properties of their host galaxy, like the star formation rate (SFR) or stellar mass ( $M_*$ ; Springel & Hernquist 2003; Oppenheimer & Davé 2006; Somerville & Davé 2015).

The mass and energy outflow rates are challenging to observe. Outflows are diffuse structures with uncertain geometries that span different ionization states and metallicities (Heckman et al. 1990, 2000; Veilleux et al. 2005), which are challenging to observationally constrain. Many studies use a single absorption line to trace both the density and kinematic information of the outflowing gas, but rely on assumptions for the ionization corrections, metallicities, and outflow radii to derive mass outflow rates (Rupke et al. 2005; Martin 2005; Weiner et al. 2009; Rubin et al. 2014; Heckman et al. 2015). These assumptions may introduce an order of magnitude scatter into the observed relations (Murray et al. 2007).

In a series of papers we have used a sample of nearby star-forming galaxies with ultraviolet spectra from the Cosmic Origins Spectrograph (COS; Green et al. 2012) on the *Hubble Space Telescope* to characterize the physical conditions within galactic outflows. In Chisholm et al. (2015) (hereafter Paper I), we define a sample of 48 nearby star-forming galaxies, our method to fit the stellar continuum, and characterize the absorption kinematics. We then use the Si II absorption profiles to find shallow scaling relations between outflow velocities and their host galaxy properties. In

\* Contact email: John.Chisholm@unige.ch

Galaxy name	$\log(M_*)$ [ $\log(M_\odot)$ ]	$v_{\text{circ}}$ [ $\text{km s}^{-1}$ ]	SFR [ $M_\odot \text{ yr}^{-1}$ ]	SFR <sub>COS</sub> [ $M_\odot \text{ yr}^{-1}$ ]	$\log(\text{O}/\text{H})+12$ [dex]	Proposal ID	References
SBS 1415+437	6.9	18	0.02	0.02	7.6	11579	8
1 Zw 18	7.2	21	0.02	0.02	7.2	11579	8
MRK 1486	9.3	82	3.6	2.5	8.1	12310	2, 6, 10, 11, 12
KISSR 1578	9.5	94	3.7	2.1	8.1	11522	3, 14
Haro 11	10.1	137	26	12	8.1	13017	1, 7
NGC 7714	10.3	156	9.2	3.1	8.5	12604	4, 5, 13
IRAS 08339+6517	10.5	179	14	4.7	8.5	12173	9
NGC 6090	10.7	202	25	5.5	8.8	12173	9

**Table 1.** Derived galaxy properties (see § 2.1 for sample selection details). The first column gives the name of the galaxy, the second column gives the stellar mass ( $M_*$ ), the third column gives the circular velocity of the galaxy ( $v_{\text{circ}}$ ) calculated using a Tully-Fischer relation (Reyes et al. 2011), the fourth column gives the star formation rate of the entire galaxy (SFR), the fifth column corrects the total SFR for the fact that COS resolves a portion of the total galaxy (SFR<sub>COS</sub>), the sixth column is the oxygen abundances ( $\log(\text{O}/\text{H})+12$ ) taken from Chisholm et al. (2015), the seventh column is the HST proposal ID, and the last column lists previous references for the data that we use. References for the targets are coded as: (1) Alexandroff et al. (2015), (2) Duval et al. (2016), (3) France et al. (2010), (4) Fox et al. (2013), (5) Fox et al. (2014), (6) Hayes et al. (2014), (7) Heckman et al. (2015), (8) James et al. (2014), (9) Leitherer et al. (2013), (10) Östlin et al. (2014), (11) Pardy et al. (2014), (12) Rivera-Thorsen et al. (2015), (13) Richter et al. (2013), and (14) Wofford et al. (2013).

Galaxy name	$\dot{M}_o/\text{SFR}_{\text{COS}}$	$\dot{E}_o/\dot{E}_{\text{SFR}}$	$\dot{p}_o/\dot{p}_{\text{SFR}}$	$M_o$ ( $10^6 M_\odot$ )	$R_i$ (pc)
SBS 1415+437	$19 \pm 17$	$0.21 \pm 0.18$	$5.7 \pm 5.0$	0.2	40
1 Zw 18	$11 \pm 8.0$	$0.15 \pm 0.11$	$3.7 \pm 2.6$	0.3	62
MRK 1486	$0.91 \pm 0.33$	$0.03 \pm 0.01$	$0.48 \pm 0.18$	1	45
KISSR 1578	$2.0 \pm 0.57$	$0.09 \pm 0.03$	$1.27 \pm 0.35$	2	54
Haro 11	$1.2 \pm 0.51$	$0.05 \pm 0.02$	$0.70 \pm 0.29$	14	101
NGC 7714	$0.23 \pm 0.08$	$0.009 \pm 0.003$	$0.13 \pm 0.04$	0.34	33
IRAS 08339+6517	$0.07 \pm 0.03$	$0.007 \pm 0.004$	$0.06 \pm 0.03$	0.02	13
NGC 6090	$0.54 \pm 0.18$	$0.02 \pm 0.006$	$0.28 \pm 0.09$	1.9	63

**Table 2.** Derived outflow properties. The first column gives the name of the galaxy, the second column gives the maximum mass outflow rate divided by the SFR in the COS aperture ( $\dot{M}_o/\text{SFR}_{\text{COS}}$ ), the third column the maximum energy outflow rate divided by the energy from supernovae within the COS aperture ( $\dot{E}_o/\dot{E}_{\text{SFR}}$ ), the fourth column gives the maximum momentum outflow rate divided by the direct momentum from supernovae within the COS aperture ( $\dot{p}_o/\dot{p}_{\text{SFR}}$ ), the fifth column gives the mass at the inner radius of the outflow, and the last column gives the inner radius of the outflow. We calculate the errors using a Monte Carlo method (see § 3.3 for details). All the values for IRAS 08339+6517 are upper limits because the profile is not fit by our model, and we exclude this galaxy from the sample (see § 4.3).

Chisholm et al. (2016a) (hereafter Paper II) we extend this analysis to the O I, Si III, and Si IV transitions, which span a factor of three in ionization potential, and probe both neutral and ionized gas. We find that the moderately ionized Si IV and neutral O I are co-moving, implying that we are observing a single outflowing structure. We then use the equivalent width ratios to study the ionization structure of the outflows, and find that the outflow equivalent widths are reproduced by photoionization models, if the observed O and B stars ionize the outflow. Using these photoionization models, we estimate the ionization structure, the metallicity, and the total hydrogen density at the base of the outflow. These values vary from galaxy-to-galaxy, and each galaxy requires a unique photoionization model. Finally, in Chisholm et al. (2016b) (hereafter Paper III) we fit detailed models of the Si IV 1402 Å line profile to determine the acceleration, the radial density structure, and the inner radius of the outflow from the starburst NGC 6090. We combine these measurements with detailed photoionization models to derive a velocity resolved mass outflow rate with observationally motivated values for the metallicity, ionization correction, and physical extent of the outflow.

Here, we extend the analysis of Paper III to a sample of 7 nearby star-forming galaxies with the highest signal-to-noise UV spectra. We first briefly describe the data analysis and how we characterize the outflow (§ 2). In § 3.2, we then examine the physical picture suggested by the observations, and use it to inform our calculation of

the mass, momentum, and energy outflow rates (§ 3.3). In § 3.3.1 we normalize the outflow energetics by the mass and energy produced by supernovae, and explore the scaling relations with the stellar mass of the galaxies. Finally, in § 4 we compare the values to previous observations and simulations (§ 4.1), explore the implications of these relations for driving galactic outflows (§ 4.2), and discuss a galaxy that our model does not fit (§ 4.3). In a companion paper, we will explore how the physical properties of galactic outflows (metallicity, density, radius and velocity structure) scale with host galaxy properties, and their implications for the mass-metallicity relation and the enrichment of the circum-galactic medium.

## 2 DATA AND ANALYSIS

The data reduction and methods follow Paper I and Paper III. Here we summarize the major steps taken, but refer the reader to those papers for details. We first discuss the sample (§ 2.1), the data reduction, and the continuum fitting (§ 2.2). We then discuss how we fit the line profiles of the Si IV 1402 Å doublet to derive important velocity-resolved relations (§ 2.3). Finally, in § 2.4 we describe how we use O I 1302 Å, Si II 1304 Å, S II 1250 Å, and Si IV 1402 Å column densities, along with CLOUDY photoionization models, to derive the metallicities, densities, and ionization corrections of the outflows.

## 2.1 Sample selection

We select the eight galaxies from Paper I that have COS spectra with a signal-to-noise ratio greater than five at 1380 Å (near the Si iv line; the median signal-to-noise ratio of the sample is 11); a measured central velocity less than 0 at the  $1\sigma$  significance for the O I 1302, Si II 1304, S II 1250, and Si IV 1402 Å lines; and are not contaminated by geocoronal emission at both the O I 1302 and Si II 1304 Å absorption lines. The most crucial, and constraining, requirement is that we cleanly observe all of the transitions because multiple transitions with different ionization potentials constrain the ionization structure and metallicity of the outflow. These cuts produce a sample of eight high-quality spectra that are kinematically defined as outflows. A list of the previous *Hubble Space Telescope* proposal identifications and references for each galaxy is given in Table 1.

Since COS is a circular aperture spectrograph, the spectral resolution varies depending on the size of the target, with the resolution of our sample varying from 21 km s<sup>-1</sup> to 58 km s<sup>-1</sup>, as measured from the Milky Way absorption lines (Paper I). In Paper I we calculate the star formation rates (SFR) and stellar masses ( $M_*$ ) of the host galaxies, assuming a Chabrier initial mass function (Chabrier 2003), using archival *WISE* (Wright et al. 2010) and *GALEX* (Martin et al. 2005) observations (Buat et al. 2011; Jarrett et al. 2013; Querejeta et al. 2015). These values are recorded in Table 1. While the sample is small, it represents the only high signal-to-noise spectra in the HST archive for which we can accurately calculate the mass outflow rates.

## 2.2 Observations and continuum fitting

The COS spectra are processed through the CalCOS pipeline, version 2.20.1, and downloaded from the MAST server. The individual exposures are combined and wavelength calibrated following the methods outlined in Wakker et al. (2015). The spectra are normalized, binned by 5 pixels (a spacing of 10 km s<sup>-1</sup>), and smoothed by 3 pixels.

A linear combination of multi-age, fully theoretical STARBURST99 models (Leitherer et al. 1999, 2010), computed using the WM-Basic stellar library and the Geneva stellar evolution tracks with high-mass loss (Meynet et al. 1994), are fit to the spectra following the methods of Paper I. We simultaneously fit for the reddening along the line-of-sight using a Calzetti extinction law (Calzetti et al. 2000). We use these fits to remove contributions from the stellar continuum, set the zero-velocity of the absorption lines, and to describe the number of ionizing photons in the photoionization models below.

## 2.3 Line profile fitting

For each galaxy we simultaneously fit the velocity-resolved Si iv optical depth ( $\tau$ ) and covering fraction ( $C_f$ ) to describe the variation of the line profile with velocity. The radiative transfer equation defines the flux ( $F$ ) at a given velocity in terms of the  $C_f$  and the  $\tau$  at that velocity as

$$F(v) = 1 - C_f(v) + C_f(v)e^{-\tau(v)} \quad (1)$$

If there is a doublet, where the transitions share the same  $C_f$  and the ratio of the two optical depths is equal to the ratio of their  $f$ -values, then a system of equations solves for both  $C_f$  and  $\tau$  independently (Hamann et al. 1997). We use the Si iv doublet to form a system of

equations and solve for the velocity-resolved  $C_f$  and  $\tau$  in terms of the flux of the Si iv doublet as

$$C_f(v) = \frac{F_W(v)^2 - 2F_W(v) + 1}{F_S(v) - 2F_W(v) + 1} \quad (2)$$

$$\tau(v) = \ln \left( \frac{C_f(v)}{C_f(v) + F_W(v) - 1} \right)$$

Where  $F_W$  is the STARBURST99 continuum normalized flux of the weaker doublet line (Si iv 1402Å), and  $F_S$  is the continuum normalized flux of the stronger doublet line (Si iv 1394Å). The  $\tau$  and  $C_f$  errors are calculated by varying the observed fluxes by a Gaussian kernel centered on zero with a standard deviation equal to the error on the flux measurement. We then recalculate the  $\tau$  and  $C_f$  values at each velocity interval, and repeat the procedure 1000 times to form  $\tau$  and  $C_f$  distributions. We take the standard deviation of these distributions as the velocity-resolved  $\tau$  and  $C_f$  errors. To increase the signal-to-noise ratio, we further bin these profiles by two pixels. The  $\tau$  and  $C_f$  distributions for each galaxy are shown in § A. Now, we fit physically motivated, velocity-resolved models to the observed  $\tau$  and  $C_f$  distributions.

To fit the  $\tau$  profile we assume that the Si iv density ( $n_4$ ) follows a radial power-law such that

$$n_4(r) = n_{4,0} \left( \frac{r}{R_i} \right)^\alpha \quad (3)$$

where  $n_{4,0}$  is the Si iv density at the base of the outflow,  $R_i$  is the initial radius of the outflow, and  $\alpha$  is an unknown power-law exponent. As discussed in Paper III, a power-law distribution with  $\alpha = -2$  is expected if the outflow is mass-conserving. In this scenario, the density falls as  $1/r^2$  as the mass in a thin shell is spread over a successively larger surface area as it moves out in the flow. This radial decline may be due to either deviations in geometry from spherically symmetric outflow geometries or because mass is removed from the flow as it propagates outward. In the local galaxy M 82, Leroy et al. (2015) find a steep density power-law, with an  $\alpha$  between  $-3$  and  $-5$ , implying that the outflow is not a mass-conserving flow. Therefore, Equation 3 is general, and allows for either a mass-conserving outflow ( $\alpha = -2$ ) or one that does not conserve mass ( $\alpha < -2$ ).

Since  $C_f$  measures the fraction of the continuum area covered by the absorbing gas,  $C_f$  will change as the solid angle of the absorbing clouds change (Martin & Bouché 2009; Steidel et al. 2010). We fit the covering fraction with a radial power-law such that

$$C_f(r) = C_f(R_i) \left( \frac{r}{R_i} \right)^\gamma \quad (4)$$

where  $C_f(R_i)$  is the covering fraction of the outflow at  $R_i$ , and  $\gamma$  is the power-law exponent that measures the decline of  $C_f$  with radius. As gas moves away from the continuum source, the total area at a given radius increases. If the clouds remain the same size, this geometric dilution will cause  $C_f$  to fall as  $r^{-2}$ . However, if the clouds expand adiabatically some of the geometric dilution can be offset, and  $C_f$  declines more gradually. In Paper III, we measure a  $\gamma$  of  $-0.8$  from the Si iv profile of NGC 6090, consistent with expectations of adiabatically expanding clouds in an adiabatically expanding medium. Moreover, Steidel et al. (2010) fit the  $C_f$  profiles of  $z \approx 2$  Lyman Break Galaxies and find  $\gamma$  values between  $-0.2$  and  $-0.6$ .

The radial velocity structure of these lines are unknown, a priori, and we assume that the velocity follows a  $\beta$ -law (Lamers &

Cassinelli 1999) such that

$$v(r) = v_\infty \left(1 - \frac{R_i}{r}\right)^\beta \quad (5)$$

where  $v_\infty$  is the measured terminal velocity of the outflow. A  $\beta$ -law is commonly used to describe stellar winds (Lamers & Cassinelli 1999). Analytic relations from Murray et al. (2005) suggest that driving outflows with optically thin radiation pressure or ram pressure lead to a  $\beta$  near  $-0.5$ , consistent with the Si iv profile from NGC 6090 Paper III. We simplify Equations 3-5 by introducing the normalized quantities  $w = v/v_\infty$  and  $x = r/R_i$  to give the relation for the normalized velocity as  $w = (1 - 1/x)^\beta$ .

As found in Paper III, the equivalent width ratios of the Si iv 1394Å and Si iv 1402Å lines indicate that the Si iv is not heavily saturated. Therefore, we simultaneously fit the observed velocity resolved optical depth and covering fraction, assuming a Sobolev optical depth (Sobolev 1960; Lamers & Cassinelli 1999; Prochaska et al. 2011; Scarlata & Panagia 2015), as

$$\tau(w) = \frac{\pi e^2}{mc} f \lambda_0 \frac{R_i}{v_\infty} n_{4,0} x^\alpha \frac{dx}{dw} = \tau_0 \frac{w^{1/\beta-1}}{\beta(1-w^{1/\beta})^{2+\alpha}} \quad (6)$$

$$C_f(w) = \frac{C_f(R_i)}{(1-w^{1/\beta})^\gamma}$$

where  $m$  is the mass of the electron,  $f$  is the oscillator strength of the Si iv 1402Å line,  $\lambda_0$  is the restframe wavelength of the Si iv 1402Å line, and  $\tau_0$  is a constant term that we define as

$$\tau_0 = \frac{\pi e^2}{mc} f \lambda_0 \frac{R_i}{v_\infty} n_{H,0} \chi_{Si4}(Si/H) \quad (7)$$

where we have replaced  $n_{4,0}$  with the hydrogen density at the base of the outflow ( $n_{H,0}$ ), the Si iv ionization fraction of the outflow ( $\chi_{Si4}$ ), and the silicon to hydrogen abundance of the outflow (Si/H). These parameters are estimated from the observed column densities and CLOUDY models in § 2.4 below.

We fit Equation 6 to the velocity resolved  $\tau$  and  $C_f$  distributions of the Si iv 1402Å line using MPFIT (Markwardt 2009) to solve for  $\tau_0$ ,  $\beta$ ,  $\alpha$ ,  $\gamma$ ,  $C_f(R_i)$ . Resonance emission decreases the  $C_f$  and increases the  $\tau$  of the outflow (Prochaska et al. 2011), leading to unphysical velocity distributions if the resonance emission is not accounted for (see gray points in § A). As in Paper III, we use the Si ii\* 1194Å non-resonant emission line as a proxy of resonance emission, and mask-out velocities with observed Si ii 1194Å emission. The Si ii\* emission lines are narrow, and typically only occupy the inner  $\pm 50$  km s<sup>-1</sup> of the profile. Therefore, low velocity absorption—which can also be contaminated with ISM absorption from within the host galaxy—is largely excluded from the fit. The fitted relations describe the velocity structure of the outflowing Si iv gas, and the profile fits for the full sample are described fully in a future paper but are shown in § A. While most galaxies have similar fit parameters (median plus standard deviation for  $\beta$ ,  $\gamma$ ,  $\alpha$  are  $0.5 \pm 0.1$ ,  $-0.9 \pm 0.7$ ,  $-5.3 \pm 2.4$  respectively), one galaxy, IRAS 08339+6517, has a  $C_f$  distribution which cannot be fit by Equation 6 (see Figure A7). Instead we force a flat unity  $C_f$  distribution ( $\gamma = 0$  and  $C_f(R_i) = 1$ ). Since IRAS 08339+6517 does not follow Equation 6, we exclude it from our outflow discussion, but include an upper limit of its mass outflow rate using  $\gamma = 0$  and  $C_f(R_i) = 1$  on all plots as an X. In § 4.3 we discuss this profile further.

## 2.4 Photoionization modeling

The column densities of the different transitions trace the ionization structure of the outflow. To characterize this ionization structure, we measure column densities ( $N$ ) of the O i 1302Å, Si ii 1304Å, S ii 1250Å, and Si iv 1402 Å lines. The measured lines are weak: the Si iv doublet equivalent width ratio is greater than 1.3 for all galaxies (median of 1.7), while the  $f$ -value ratio is 2.0, indicating that the Si iv 1402Å line is not overly saturated. We measure column densities assuming that the lines are partially covered, as measured by  $C_f(R_i)$  in Equation 6. Partial coverage is important, especially for low-mass galaxies with low covering fractions; not accounting for partial coverage artificially decreases  $N$ . We determine  $N$  by integrating the optical depth over a by-eye determined velocity range using the following expression

$$N = \frac{3.77 \times 10^{14} \text{ cm}^{-2}}{\lambda[\text{Å}]f} \int \ln \left( \frac{C_f(R_i)}{C_f(R_i) + F(v) - 1} \right) dv \quad (8)$$

where  $F(v)$  is the STARBURST99 stellar continuum normalized flux. We assume that  $C_f(R_i)$  remains the same for each of the four transitions, consistent with the result from Paper II that the line width, not the covering fraction, changes from transition to transition.

We fit the observed column densities to integrated column densities from a large grid of CLOUDY, version 13.03, photoionization models (Ferland et al. 2013), which use the observed STARBURST99 stellar continuum fit as the ionizing source. Additionally, we use an expanding spherical geometry with the measured density profiles from § 2.3. We create the CLOUDY models by varying the ionization parameter, metallicity, and density of the outflow; and tabulate the column densities for each model. We use CLOUDY's H ii abundances, including the Orion dust grain distribution which accounts for depletion of metals onto grains, from Baldwin et al. (1991). We scale these abundances between  $0.01 Z_\odot$  and  $2.5 Z_\odot$  to create the grid of CLOUDY models. We then infer the best-fit ionization parameters, metallicities, and densities using a Bayesian approach with the O i, Si ii, S ii, and Si iv column densities from the observations and the CLOUDY models (Paper III). From these models we estimate  $\chi_{Si4}$ , the outflow metallicity ( $Z_0$ ), and  $n_{H,0}$ . The ionization fractions and metallicities convert  $n_{H,0}$  to the Si iv density at the base of the outflow ( $n_{4,0}$ ), which, with the fitted Si iv optical depth and maximum Si iv outflow velocity, defines  $R_i$  (see Equation 7; Paper III). We can now calculate the masses and energetics of the outflows.

## 3 MASSES AND ENERGETICS OF OUTFLOWS

Here we calculate the mass outflow rates and energetics of the galactic outflows. In § 3.1 we consider what drives the outflows: energy and momentum from star formation. By comparing the outflow mass, momentum and energy to the corresponding quantities released through star formation, we study how efficiently outflows remove mass and momentum from galaxies. We then consider the physical situation of galactic outflows by asking: on which physical scales do we observe outflows (§ 3.2)? The answer to this question affects how we interpret the energetics of the outflows. Finally, in § 3.3 we calculate the mass outflow rates ( $\dot{M}_o$ ), energy outflow rates ( $\dot{E}_o$ ), and momentum outflow rates ( $\dot{p}_o$ ); and derive how these quantities scale with the stellar mass of the galaxy (§ 3.3.1).



### 3.1 Energetics of star formation

Star formation deposits energy and momentum into gas, accelerating it out of star-forming regions (McKee & Ostriker 1977; Dekel & Silk 1986; Murray et al. 2005). Therefore, to know the efficiency of a galactic outflow one must know the amount of energy deposited into the surrounding gas by star formation. For example, comparing  $\dot{M}_0$  to the mass of stars formed per unit time (SFR) describes how efficiently galaxies convert gas into stars. The ratio of  $\dot{M}_0$  to SFR is called the mass-loading factor. Similarly, we normalize the momentum and energy of the outflow by the momentum and energy released by star formation. Leitherer et al. (1999) give the energy deposition rate from supernovae as

$$\dot{E}_{\text{SFR}} = 3 \times 10^{41} \left( \frac{\text{SFR}}{1 M_{\odot} \text{ yr}^{-1}} \right) \text{ g cm}^2 \text{ s}^{-3} \quad (9)$$

and Murray et al. (2005) give the direct momentum deposition from supernovae as

$$\dot{p}_{\text{SFR}} = 2 \times 10^{33} \left( \frac{\text{SFR}}{1 M_{\odot} \text{ yr}^{-1}} \right) \text{ g cm s}^{-2} \quad (10)$$

Where both of these relations assume one supernovae per 100  $M_{\odot}$  of stars formed. These relations only include the direct energy and momentum from supernovae; other energy and momentum sources may change these relations. For  $\dot{p}_{\text{SFR}}$ , radiation pressure, the Sedov Taylor phase, and stellar winds from massive stars inject at least as much momentum as supernovae (Leitherer et al. 1999; Kim & Ostriker 2015). Below, we normalize the mass, momentum and energy outflow rates by their star formation quantities to study how efficiently outflows remove mass, momentum and energy from star-forming regions.

### 3.2 Which physical scales are outflows observed?

Our observations indicate that the covering fraction declines with radius ( $C_f \propto r^{-0.9}$ ) and the observed gas density drops dramatically with radius ( $n \propto r^{-5.3}$ ). Further, the measured initial radii of the outflows indicate that they begin nearly at the size of the star-forming regions. However, this does not mean that there is not absorption from larger radii along the line-of-sight. The equivalent widths of our outflows are typically 6-10 times larger than the equivalent widths seen from studies of the circum-galactic medium (Steidel et al. 2010; Werk et al. 2013). This means that the circum-galactic absorption is likely blended within the outflow absorption at low, zero, or positive velocities, contaminating trends of outflow centroid velocities, as discussed in Paper I. While warm gas has been observed out to 100 kpc in the circum-galactic medium (Steidel et al. 2010; Tumlinson et al. 2011; Werk et al. 2014), a majority of the gas we observe at high velocities ( $< -200 \text{ km s}^{-1}$ ) likely comes from within 300 pc of the star-forming region (Paper III).

Recently, Thompson et al. (2016) proposed a plausible scenario that links outflows at small radii to circum-galactic absorption at large radii. High-energy photons, stellar winds, and supernovae inject energy and momentum into the surrounding gas, thermalizing some gas into a hot,  $10^7 \text{ K}$ , outflow and accelerating the residual gas out of the star-forming region (Weaver et al. 1977; Chevalier & Clegg 1985; Heckman et al. 2000; Cooper et al. 2008; Bustard et al. 2016). The cooler photoionized gas observed here is produced either during the snowplow phase of the hot supernovae ejecta (McKee & Ostriker 1977; Mac Low et al. 1989), or it is ambient gas entrained in the hot outflow (Cooper et al. 2009). Either way, the photoionized

gas is radially accelerated, destroyed and incorporated into the hotter outflow on short timescales (Klein et al. 1994; Scannapieco & Brüggén 2015; Brüggén & Scannapieco 2016). This process "mass-loads" the wind, increasing the mass of the hot outflow (Strickland & Heckman 2009), and accounts for the rapid drop in Si IV density (see § 2.3; Paper III). The hot mass-loaded phase continues out of the disk, where it encounters and interacts with the hot ejecta from other localized star-forming regions, producing the shocked shell-like structures and filaments seen in recombination lines in M 82 (Shopbell & Bland-Hawthorn 1998). This hotter outflow continues out of the galaxy, undetected by the photoionized tracers here, adiabatically and radiatively cooling as it travels out. Eventually the hot outflow cools to temperatures near the peak of the cooling curve where it shocks, reproducing photoionized gas at large radii (Thompson et al. 2016).

This physical picture means that the observed outflows are powered by the local star formation within the COS aperture, and the outflow properties depend on the local star formation (Bordoloi et al. 2016). Consequently, the driving source of the outflow is not the global SFR, rather the local SFR. Our global SFRs are calculated from a combination of the FUV and FIR luminosities (Paper I). We cannot use this method for the local SFRs because we lack high-resolution FUV and FIR imaging. However, we can measure the FUV in our aperture directly from the COS spectra. Assuming that the fraction of unobscured-to-total SFR is the same in the COS aperture as in the galaxy as a whole we calculate:

$$\text{SFR}_{\text{COS}} = \text{SFR} \times \frac{F_{\text{COS}}}{F_{\text{GALEX}}} \quad (11)$$

Where SFR is the total SFR calculated using the IR and UV luminosities,  $F_{\text{COS}}$  is the flux in the COS aperture, and  $F_{\text{GALEX}}$  is the *GALEX* measured flux. The lowest mass galaxies have similar  $\text{SFR}_{\text{COS}}$  to their total SFR because the COS aperture encloses all of the *GALEX* flux, whereas the higher mass galaxies have spatially extended star formation outside of the COS aperture. This model assumes that the IR light follows the UV light, whereas the SFR of high-mass galaxies may be clumpy.  $F_{\text{COS}}/F_{\text{GALEX}}$  ranges from 1, for low-mass galaxies, to 0.22, for the highest mass galaxies. The  $\text{SFR}_{\text{COS}}$  values for the full sample are given in Table 1.

### 3.3 Mass and energy outflow rates

Here we estimate the mass, energy, and momentum outflow rates. In Paper III, we calculate the mass outflow rate ( $\dot{M}_0$ ) at each velocity interval using the profile fitting and the photoionization modelling as

$$\dot{M}_0(r) = \Omega C_f(r) v(r) \rho(r) r^2 \quad (12)$$

$$\dot{M}_0(w) = \Omega C_f(R_i) v_{\infty} \mu m_p n_{\text{H},0} R_i^2 \frac{w}{(1 - w^{1/\beta})^{2+\gamma+\alpha}}$$

Where  $\mu m_p$  is the average mass per nucleon, or 1.4 times the proton mass for standard abundances (Asplund et al. 2009);  $w$  is the velocity normalized by  $v_{\infty}$ ; and  $\Omega$  is the solid angle occupied by the outflow, which we assume is  $4\pi$  because a locally driven outflow is not yet collimated by the disk. The relations for  $C_f(r)$  and  $\rho(r)$  are taken from the profile fitting (Equation 2 and Equation 3), and the values for  $n_{\text{H},0}$  and  $R_i$  are taken from the photoionization modeling (§ 2.4) and Equation 7, respectively. The total mass at each velocity interval is similarly calculated as

$$M_0(w) = \Omega C_f(R_i) \mu m_p n_{\text{H},0} R_i^3 \left( \frac{1}{1 - w^{1/\beta}} \right)^{3+\alpha+\gamma} \quad (13)$$

We then calculate the energy outflow rate ( $\dot{E}_o$ ) using Equation 12 as

$$\dot{E}_o(w) = \frac{1}{2} \dot{M}_o(w) v_{\infty}^2 w^2 \quad (14)$$

and the momentum outflow rate ( $\dot{p}_o$ ) as

$$\dot{p}_o(w) = \dot{M}_o(w) v_{\infty} w \quad (15)$$

These four quantities are velocity resolved. Specifically,  $\dot{M}_o$  increases at low-velocities and decreases at high-velocities, reaching a maximum  $\dot{M}_o$  at intermediate velocities. The increase in  $\dot{M}_o$  happens as the velocity and radius increase, and the decrease happens as the density and covering fraction decrease (Paper III). Here, we take the maximum value of each quantity as the estimate of the quantity. This means that the reported values in Table 1 and in each figure are calculated at specific velocities that correspond to their maximum values. We choose the maximum value as the representative value because a radially accelerated outflow implies that the  $\dot{M}_o$  in each velocity interval is a snapshot of the  $\dot{M}_o$  at a given velocity (or equivalently radius or time). Further, if the decrease in density is due to a phase change (photoionized gas to a hotter phase), then the decrease in  $\dot{M}_o$  actually represents a transfer of  $\dot{M}_o$  from the photoionized phase to a hotter phase. In this case, the maximum  $\dot{M}_o$  represents the time when the photoionized outflow is the largest contributor to the total  $\dot{M}_o$  of the galaxy.

The errors of each quantity are calculated by varying the estimated parameters of Equation 12 by a Gaussian distribution centered on zero with a standard deviation corresponding to the parameters' measured errors. We then recalculate the  $\dot{M}_o$  value with these Monte Carloed values, and repeat the procedure 1000 times to form a  $\dot{M}_o$  distribution. We take the standard deviation of this distribution as the errors on  $\dot{M}_o$  and propagate the errors accordingly for  $\dot{p}_o$  and  $\dot{E}_o$ . The errors are larger for low-mass galaxies because narrow absorption line profiles are challenging to determine the density scaling ( $\alpha$ ), which leads to larger uncertainties in  $\alpha$  and  $\dot{M}_o$ . We normalize each of the quantities by the SFR, star formation energy deposition rate (Equation 9) and star formation momentum deposition rate (Equation 10) within the COS aperture to determine how efficiently outflows remove these quantities from star-forming regions (see Table 2 for the values).

### 3.3.1 Scaling relations

Here, we study how the masses and energetics of outflows scale with the stellar mass of their host galaxies. With only a sample of seven galaxies, more high-quality data is required to confirm these relations, but we do find statistically significant correlations. As discussed in § 4.3, we exclude IRAS08339 from the fits because the line profile does not follow the model of § 2.3, and upper-limits of the  $\dot{M}_o$  estimates are shown on the plots as an X, assuming  $\gamma = 0$  and  $C_f(R_i) = 1$ . Figure 1 shows the scaling of the mass-loading factor with stellar mass. Over-plotted in black is the least-squares fit to the relation, with the 95% confidence interval as the gray region. This trend corresponds to a relation of

$$\frac{\dot{M}_o}{\text{SFR}_{\text{COS}}} = 0.76 \pm 0.20 \left( \frac{M_*}{10^{10} M_{\odot}} \right)^{-0.43 \pm 0.07} \quad (16)$$

The fit is significant at the  $3\sigma$  significance level (p-value < 0.001), and has a coefficient of determination ( $R^2$ ) of 0.88, where an  $R^2$  of 1.0 implies that the fit describes 100% of the variation. The relation has a residual standard error of 0.26 dex.

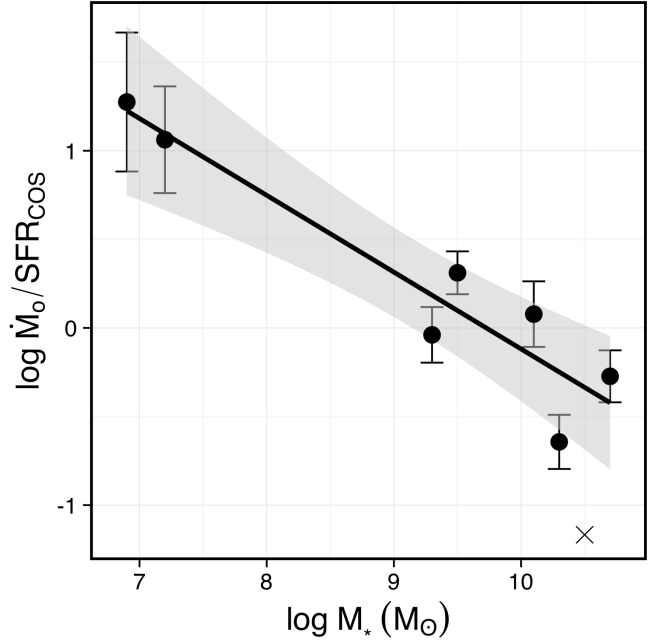


**Figure 1.** The scaling of the maximum mass-loading factor ( $\dot{M}_o/\text{SFR}_{\text{COS}}$ ) with stellar mass ( $M_*$ ). The line gives the least squares regression fit to the circles (see Equation 16), while the gray region is the 95% confidence interval of the fit. The X is IRAS 08339+6517, a high-mass merger that is not fit by the line profile model of Equation 6 (see § 4.3).

Several simulations scale the mass-loading factor by the circular velocity ( $v_{\text{circ}}$ ) of the galaxy (e.g., Somerville & Davé 2015). Since we do not measure  $v_{\text{circ}}$  for our sample, we rescale  $M_*$  into  $v_{\text{circ}}$  using the Tully-Fisher relation from Reyes et al. (2011). Doing this, we find

$$\frac{\dot{M}_o}{\text{SFR}_{\text{COS}}} = 1.12 \pm 0.27 \left( \frac{v_{\text{circ}}}{100 \text{ km/s}} \right)^{-1.56 \pm 0.25} \quad (17)$$

Similarly, Figure 2 gives the scaling of the momentum efficiency with  $M_*$  as

$$\begin{aligned} \frac{\dot{p}_o}{\dot{p}_{\text{SFR}}} &= 0.42 \pm 0.12 \left( \frac{M_*}{10^{10} M_{\odot}} \right)^{-0.36 \pm 0.07} \\ &= 0.58 \pm 0.15 \left( \frac{v_{\text{circ}}}{100 \text{ km/s}} \right)^{-1.39 \pm 0.26} \end{aligned} \quad (18)$$

which is significant at the  $2.5\sigma$  level (p-value < 0.006), and has an  $R^2$  of 0.85. Finally, in Figure 3 we show the variation of the outflow energy efficiency with  $M_*$ , which has a scaling relation of

$$\begin{aligned} \frac{\dot{E}_o}{\dot{E}_{\text{SFR}}} &= 0.03 \pm 0.01 \left( \frac{M_*}{10^{10} M_{\odot}} \right)^{-0.28 \pm 0.07} \\ &= 0.04 \pm 0.01 \left( \frac{v_{\text{circ}}}{100 \text{ km/s}} \right)^{-1.02 \pm 0.27} \end{aligned} \quad (19)$$

This relation is only significant at the  $2\sigma$  level (p-value < 0.01), and has an  $R^2$  of 0.74. We do not consider this relation significant, but an inverse relation exists such that low-mass galaxies have higher energy efficiencies (the trend has a Kendall's  $\tau$  coefficient of  $-0.71$ ). These relations describe how efficiently photoionized

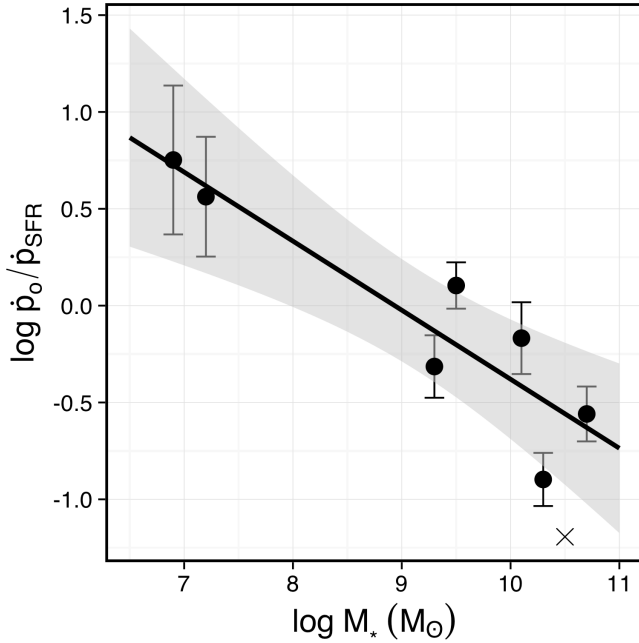


**Figure 2.** The outflow momentum efficiency ( $\dot{p}_o/\dot{p}_{\text{SFR}}$ ) with stellar mass ( $M_*$ ). The line gives the least squares regression fit to the circles (see Equation 18), while the gray region is the 95% confidence interval of the fit. The X is IRAS 08339+6517, a high-mass merger that is not fit by the line profile model of Equation 6 (see § 4.3).

outflows remove mass, momentum and energy from star-forming regions.

## 4 DISCUSSION

### 4.1 Comparison to previous observations and simulations

The most important results of this study are the values of the mass outflow rate, the momentum outflow rate, and the energy outflow rate (Table 2) that are estimated using observationally motivated values for the outflow metallicity, ionization fraction, and radius. Additionally, we use this small sample to find significant ( $>2.5\sigma$ ) scaling relations between the mass (Figure 1) and momentum (Figure 2) of the photoionized outflows and the stellar mass of their host galaxies ( $M_*$ ).

The mass-loading values found here are broadly consistent with the wide range of mass-loading factors found in the literature (Rupke et al. 2005; Weiner et al. 2009; Rubin et al. 2014). Three of the galaxies studied here are included in the Heckman et al. (2015) sample, which calculates  $\dot{M}_o$  assuming a constant outflow column density of  $10^{20.85} \text{ cm}^{-2}$ , a constant outflow metallicity of  $0.5 Z_\odot$ , and that the outflow radius is a constant factor of two times the radius of the star-forming region. Our estimates of the mass-loading factors for these three galaxies are, on average, a factor of three times smaller than theirs, however, the difference has a large range: between an over-estimate of 1.04 and 5.7 times. This discrepancy is largely due to our observationally motivated radii, metallicities, and ionization corrections (Paper III), which vary by factors of 3, 10 and 3, respectively, for the sample. Heckman et al. (2015) find a statistically weak correlation between  $\dot{M}_o/\text{SFR}$  and  $v_{\text{circ}}$  of  $\dot{M}_o/\text{SFR} = 1.8 (v_{\text{circ}}/100 \text{ km s}^{-1})^{-0.98}$ . This relation has

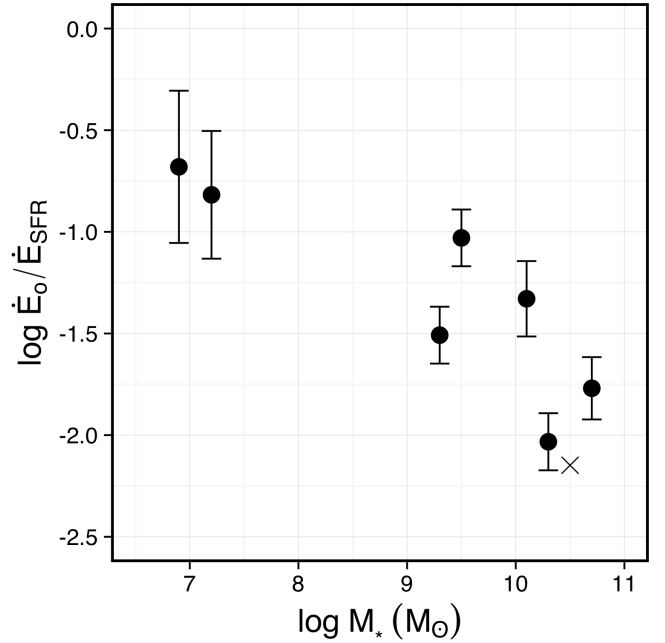


**Figure 3.** The outflow energy efficiency ( $\dot{E}_o/\dot{E}_{\text{SFR}}$ ) with stellar mass ( $M_*$ ). We do not find a significant correlation between  $\dot{E}_o/\dot{E}_{\text{SFR}}$  and  $M_*$ , although there is a trend such that higher mass galaxies have lower  $\dot{E}_o/\dot{E}_{\text{SFR}}$ . The X is IRAS 08339+6517, a high-mass merger that is not fit by the line profile model of Equation 6 (see § 4.3).

a normalization that is 1.6 times larger and a shallower scaling than Equation 17. Crucially, by not accounting for galaxy-to-galaxy variations in the metallicities, ionization corrections and radii, previous studies may introduce up to a factor of 10 scatter into the  $\dot{M}_o$  relations, possibly obscuring trends.

We also compare these results to relations typically used in simulations. Simulations use a variety of scaling relations to drive galactic outflows (Somerville & Davé 2015), including scaling the mass-loading factor as  $v_{\text{circ}}^{-1}$  (Oppenheimer & Davé 2008; Dutton 2012) or as  $v_{\text{circ}}^{-2}$  (Benson et al. 2003; Somerville et al. 2008). In Figure 4 we over-plot the Somerville et al. (2008) relation on our  $M_o$  estimates as a dot-dashed line. This relation is steeper and has a larger normalization than the observations presented here.

Recent high-resolutions simulations produce outflows without explicitly scaling the outflow properties to the host galaxy. One example of this is the FIRE simulation (Hopkins et al. 2014), which finds the mass-loading factor to scale as  $M_*^{-0.35}$  when they calculate  $\dot{M}_o$  at  $0.25 R_{\text{vir}}$  (Muratov et al. 2015), as shown by the dashed line in Figure 4. The scaling of this relation is statistically similar to Equation 16, but the normalization is 4.6 times larger. However, we caution that the value of  $\dot{M}_o$  from the simulations depends on the radius used to calculate  $\dot{M}_o$ , with  $\dot{M}_o$  varying by a factor of 4 whether it is calculated at  $R_{\text{vir}}$  or at  $0.25R_{\text{vir}}$  (Muratov et al. 2015). The discrepancy between our observations and the simulations does not necessarily mean that the simulation drives outflows that are too large: if other phases like the molecular gas, O VI coronal gas, or hot X-ray-emitting plasma substantially contribute to the mass and momentum of the outflow, than our observed outflows do not account for the entire mass outflow. Future simulations that track the phase structure of outflows (e.g. molecular, photoionized, transitional, and hot gas) can compare the mass-loading factors in different ioniza-

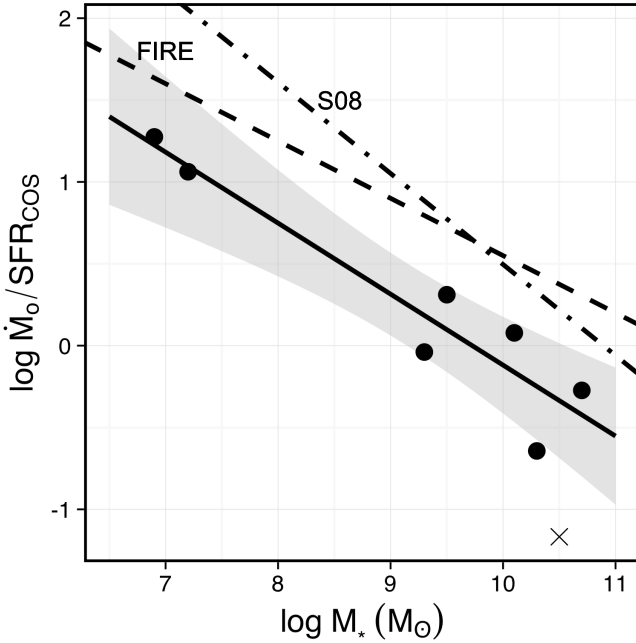


**Figure 4.** Comparison of the observed mass-loading factors ( $\dot{M}_o/\text{SFR}_{\text{COS}}$ ) with typical relations from simulations. The solid line gives the least squares regression fit to the circles (see Equation 16), while the gray region is the 95% confidence interval of the fit. The dashed line shows the best-fit relation from the FIRE simulations (calculated at  $0.25R_{\text{vir}}$ ; Muratov et al. 2015) and the dot-dashed line shows the relation from Somerville et al. (2008) (S08). The relations from simulations are typically a factor of five larger than the observed photoionized outflows. The X is IRAS 08339+6517, a high-mass merger with a line profile that is not fit by our model (see § 4.3).

tion phases to determine if the normalization discrepancy lies in unobserved phases or in the assumptions of the simulations.

#### 4.2 The energetics of driving galactic outflows

Driving galactic outflows in simulations is challenging. Cosmological simulations need to account for entire galaxies with physics on tens of kpc scales as well as detailed physics on sub-pc scales. In particular, resolving the size of a supernova blastwave is crucial to account for the energy and momentum of outflows because most of the supernova energy is radiated away in these small, dense regions when they are under-resolved (Katz 1992). The lack of resolution prompted simulations to use computational methods, like temporarily turning off cooling immediately after a supernova or converting all of the supernova energy into kinetic energy (Navarro & White 1993; Rosdahl et al. 2016), to eliminate overcooling. More recently, simulations scale the outflow velocities and mass-loading factors to parameters of the host galaxies (Benson et al. 2003; Oppenheimer & Davé 2008; Vogelsberger et al. 2013; Somerville & Davé 2015), enabling simulations to generate outflows while remaining computationally feasible.

Driving outflows using scaling relations has a logical theoretical argument: star formation transfers momentum or energy into the surrounding gas which accelerates the gas out of the galaxy. If observations can relate the transfer of momentum from star formation to the outflow, then simulations will drive realistic outflows using moderate computing resources. Typically, star formation is assumed

to drive outflows by imparting momentum to the gas as

$$\dot{p}_o = \dot{M}_o v_o = \zeta \dot{p}_{\text{SFR}} \quad (20)$$

where  $v_o$  is the outflow velocity and  $\zeta$  is the fraction of the total momentum produced by star formation ( $\dot{p}_{\text{SFR}}$ ) that is transferred to the outflow.

Our sample has large  $\zeta$  values: the median momentum of the outflow is 68% of the momentum that is directly injected by supernovae. Moreover, outflows from galaxies below  $\log(M_*)$  of 9 have more momentum than provided by supernovae alone. Stellar winds, the Sedov Taylor phase, and radiation pressure also add momentum to the gas, where STARBURST99 models imply that radiation pressure and stellar winds add at least as much momentum as supernovae (Leitherer et al. 1999). Additionally, Equation 10 may underestimate the total amount of momentum injected by supernovae by up to a factor of 10 during the Sedov-Taylor phase (Hopkins et al. 2014; Kim & Ostriker 2015; Kim et al. 2017). These phases are crucial for understanding the amount of momentum transferred to the outflow.

Regardless,  $\dot{p}_o/\dot{p}_{\text{SFR}}$  values greater than one require more sources of momentum than just the direct momentum from supernovae to produce the observed outflow momenta (Hopkins et al. 2012). The roles of different momentum sources are explored in H II regions of the Large and Small Magellanic Clouds where observations suggest that pressure from warm gas dominates the energetics, but there are also significant contributions from hot gas pressure and radiation pressure from dust at small radii (Lopez et al. 2011, 2014). At a radius of 75 pc, Lopez et al. (2014) find that the dominant pressure source changes from radiation pressure to the thermal pressure of warm gas. The lower-mass galaxies tend to have small  $R_i$  (Table 2), which may indicate that  $\dot{p}_{\text{SFR}}$  is different for these low-mass galaxies. Further, Equation 10 assumes that the observed star formation drives the observed outflows. The timescales defined by the velocity law imply that the gas is accelerated to terminal velocities in 1 – 10 Myr (Equation 5), which is shorter than the 100 Myr timescales of the IR and UV SFRs. Therefore, bursty star formation may impart different  $\dot{p}_o$  than assumed in Equation 10.

Theory typically solves Equation 20 by assuming that  $v_o$  scales linearly with  $v_{\text{circ}}$ , that  $\dot{p}_{\text{SFR}}$  is proportional to the SFR (Equation 10), and that  $\zeta$  is constant (Murray et al. 2005). Placing these assumptions into Equation 20 and solving for  $\dot{M}_o/\text{SFR}$  gives a scaling of  $v_{\text{circ}}^{-1}$ , which is often called a momentum driven outflow (Murray et al. 2005). A similar argument is made using the energy from star formation to derive the scaling of the mass-loading for an energy driven outflow as  $v_{\text{circ}}^{-2}$ . Simulations often use these relations to produce galactic outflows (§ 4.1).

However, our observations indicate that the situation is more nuanced because the momentum efficiency is not constant with  $M_*$ . The normalized momentum flux of SBS 1415+437, the lowest mass galaxy, is 20 times larger than the highest mass galaxy, NGC 6090. Furthermore, the scaling of the momentum efficiency with  $M_*$  (Equation 18) indicates that momentum is either more easily dissipated in high-mass galaxies, or star formation injects more momentum in low-mass galaxies.

Gravitational drag could dissipate momentum. For example, the inward momentum deposition due to gravity ( $\dot{p}_g$ ) is equal to the retarding force of gravity ( $F_g$ ). If we assume a spherical mass distribution, the net force on the outflow is given as

$$\dot{p}_o = \dot{p}_{\text{SFR}} - \frac{M_o v_{\text{circ}}^2}{R_i} \quad (21)$$

Assuming that the bulk of outflowing mass ( $M_o$ ) is at  $R_i$  (Paper



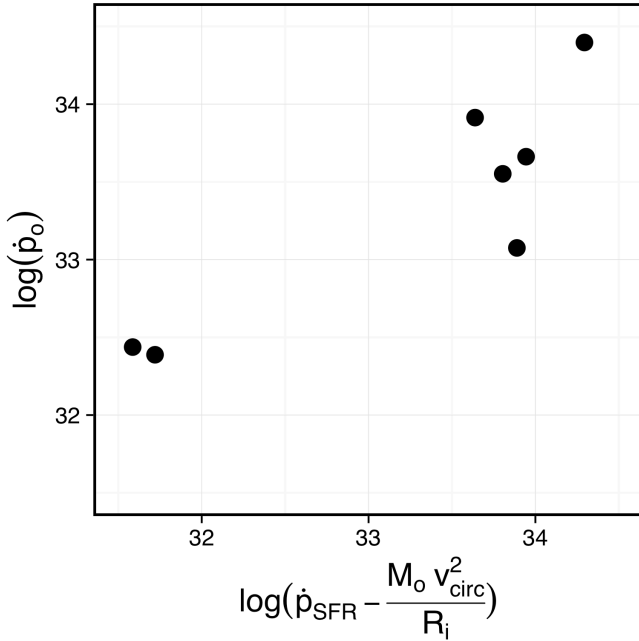


**Figure 5.** A simplified model describing the relationship between the outflow momentum ( $\dot{p}_{\text{out}}$ ; in units of  $\text{g cm s}^{-2}$ ) and the net force acting on the outflow (see Equation 21; in units of  $\text{g cm s}^{-2}$ ). This simple model uses the observed star formation momentum to accelerate the outflow while gravity counteracts this acceleration to describe the observed outflow momenta.

III), we use the  $R_i$  and  $M_o$  values from Table 2 to test whether this simplified model roughly reproduces the observed outflow momenta (Figure 5). This model does have a few limitations. First, the  $R_i$  values are sufficiently small such that the enclosed regions might not sample the full dark matter profile, and the gravitational force may not be accurately modeled by  $v_{\text{circ}}$ . The model also does not account for the fact that low-mass galaxies have larger  $\dot{p}_o$  than  $\dot{p}_{\text{SFR}}$ , implying that supernovae are not the only momentum source accelerating these outflows (see the discussion above). This fact is partially offset because low-mass galaxies have lower covering fractions, possibly reducing the total amount of  $\dot{p}_{\text{SFR}}$  transferred to the outflow. Regardless, this simplified model has a relationship that is significant at the  $3\sigma$  significance, consistent with a unity slope, an  $R^2$  of 0.85 and a Kendall's  $\tau$  coefficient of 0.89. A simple model where gravity dissipates momentum from the outflow may explain the observed decrease in  $\dot{p}_o/\dot{p}_{\text{SFR}}$  with increasing  $M_*$ .

The energy efficiencies ( $\dot{E}_o/\dot{E}_{\text{SFR}}$ ) of the outflows range between 0.9-21%, implying that most of the energy from supernovae is dissipated by gravity, radiated away, or not in the photoionized phase. The  $\dot{E}_o/\dot{E}_{\text{SFR}}$  values are consistent with the 1-10% often found in numerical simulations (Thornton et al. 1998; Efstathiou 2000). Importantly,  $\dot{E}_o/\dot{E}_{\text{SFR}}$  of the photoionized outflows increases with decreasing  $M_*$  such that low-mass galaxies drive more efficient galactic outflows than high-mass galaxies. The combination of more efficient outflows and shallower potentials means that low-mass galaxies more efficiently remove gas from their star-forming regions (Dekel & Silk 1986).

Mass-loading factors above one indicate that the outflows deplete the gas within the galaxy more than the star formation does. Equation 16 implies that the mass-loading factor exceeds one when  $\log(M_*)$  is less than 9.7. Outflows regulate the gas depletion of

low-mass galaxies; star formation regulates the gas depletion of high-mass galaxies. This critical stellar mass is similar to the stellar mass found in Paper I, below which outflow velocities are faster than escape velocities. In fact, only NGC 7714 and NGC 6090, the two highest mass galaxies in the sample, do not have Si IV absorption at velocities greater than three times their  $v_{\text{circ}}$ , a typical estimate of the escape velocity (Heckman et al. 2000). Since the outflow is accelerated radially, the model presented here defines whether outflows escape the gravitational potential differently than previous models. In fact, with a radially accelerated outflow, each velocity interval is a snapshot of the outflow in time (or radius, or velocity) which may be accelerated to higher velocities at later times. Unfortunately, the density also declines rapidly with radius, making it impossible to observe whether the outflows from the highest-mass galaxies reach the escape velocity.

Galaxies in this sample with  $\log(M_*)$  less than 9.7 have outflows that deplete more gas than their star formation does at velocities high enough to completely remove the gas from the galaxies. This may produce the bursty star formation histories of dwarf galaxies (Mateo 1998) by removing most of the gas in a single burst of star formation (Dekel & Silk 1986). Conversely, high-mass galaxies retain their outflows, and the gas reaccretes onto the galaxy as a galactic fountain (Shapiro & Field 1976), providing a secondary source of star-forming material. Consequently, galaxies must be massive to retain outflowing gas, to efficiently convert gas into stars, and to have relatively constant star formation histories. Since star formation dominates the gas depletion in galaxies with halo masses greater than  $10^{11.4} M_\odot$  (Moster et al. 2010), these galaxies retain a higher fraction of their total baryons as stars (i.e. they have a higher  $M_*/M_{\text{halo}}$  ratio). The observed  $M_*/M_{\text{halo}}$  relation peaks near  $10^{12} M_\odot$  (Moster et al. 2010) and declines at higher masses as AGN feedback becomes important, or as the halo becomes massive enough to shock heat accreting gas to high temperatures (so called hot-mode accretion; Kereš et al. 2009). Outflows are a significant component of galaxy evolution by shaping their star formation histories, regulating their gas content, and removing their baryons.

### 4.3 The curious case of IRAS 08339+6517

A curious outlier to the above trends is the high-mass merging system IRAS 08339+6517. This galaxy has an anomalously low mass outflow rate, but extremely high outflow velocity. In Paper I we define a group of outflows with maximum velocities greater than  $750 \text{ km s}^{-1}$ , that have outflow velocities 32% higher than other galaxies at similar stellar mass and SFR. IRAS 08339+6517 is the only galaxy in this sample that is in that high-velocity group. What makes IRAS 08339+6517 such a strange galaxy?

The power of the detailed profile fitting presented here is that we can differentiate groups of outflows based on the model fits to the absorption profile. The line profile of IRAS 08339+6517 does not fit the prescription in § 2.3 largely because  $C_f$  does not vary coherently with velocity, as prescribed by the power-law scaling (see Figure A7). This is in sharp contrast to the rest of the sample (see § A), which have similar  $C_f$  distributions with a  $C_f$  power-law exponent ( $\gamma$ ) of -0.88. To derive an upper limit to  $\dot{M}_o$  for IRAS 08339+6517, we set the  $C_f$  distribution by-hand to match the observations, with  $\gamma = 0$  and  $C_f(R_i) = 1$ .

In Paper III we use the observed  $C_f$  power-law scaling of  $r^{-0.8}$  to approximate the outflow as an ensemble of adiabatically expanding clouds in an adiabatically expanding medium. No variation in  $C_f$  with velocity requires that the outflowing clouds expand at the

same rate as geometric dilution. Alternatively, the high-velocity outflows might not fit the physical picture presented in § 2.3. One possibility is that the absorption does not correspond to outflowing gas, rather tidal interactions have distributed gas at a wide range of velocities along the line-of-sight, creating the unity covering of the source in Figure A7.

NGC 7552, another merger with a high-velocity outflow (Si II velocity of  $-1043 \text{ km s}^{-1}$ ), has a similarly flat Si IV  $C_F$  distribution. Unfortunately, strong geocoronal lines contaminate the O I and Si II 1304 Å profile, making photoionization models impossible for this galaxy. While two galaxies do not constitute a complete group, their similarities suggest that the highest velocity outflows have different line profiles, and including different types of outflow profiles may increase the scatter, increase measured velocities, and confuse the derivation of trends between outflow properties and host galaxy properties.

## 5 CONCLUSION

Here we calculate the mass ( $\dot{M}_o$ ), energy ( $\dot{E}_o$ ), and momentum ( $\dot{p}_o$ ) outflow rates for a sample of 7 nearby star-forming galaxies. We use a Sobolev approximation and detailed photoionization models to determine the quantities with fewer assumed parameters than previous studies. These observations describe how efficiently photoionized outflows remove mass and momentum from star-forming regions. For example, galaxies in the sample with  $\log(M_*)$  less than 9.7 eject more mass in their outflow than they form into stars, at velocities that exceed their escape velocities. The momentum of outflows from low-mass galaxies is greater than the momentum directly injected from supernovae alone, implying that there must be additional momentum sources driving the outflows. Only 1-20% of the energy released by supernovae is converted into the kinetic energy of the photoionized outflow, the rest is dissipated by gravity, radiated away, or in a different temperature phase. The values of the mass-loading factor,  $\dot{p}_o/\dot{p}_{\text{SFR}}$ , and  $\dot{E}_o/\dot{E}_{\text{SFR}}$  describe how efficiently outflows remove gas from galaxies, and demonstrate that the evolution of the gas content of low-mass galaxies is dominated by galactic outflows.

We find a  $3\sigma$  relation between the galactic stellar mass and the mass-loading factor ( $\dot{M}_o/\text{SFR}$ ; Equation 12 and Figure 1). The  $\dot{p}_o/\dot{p}_{\text{SFR}}$  ratio is also correlated at the  $2.5\sigma$  significance with  $M_*$  (Figure 2). The momenta are described by a simple model where star formation drives the gas outward while gravity counteracts the acceleration (Equation 21 and Figure 5). Additionally, low-mass galaxies are more energy efficient than high-mass galaxies, suggesting that dwarfs efficiently remove gas from their star-forming regions. The mass outflow rates presented here are five times weaker than simulations typically implement, but have similar scalings. This normalization discrepancy is likely because we only observe the photoionized outflow and there is a substantial amount of mass in other outflowing phases.

In a future paper, we will discuss how the outflow metallicity, inner radius, and density profile changes with star formation rate and stellar mass. These results are crucial to understanding the enrichment of the circum-galactic medium, and how outflows transport metals out of star-forming regions to establish the mass-metallicity relationship.

## ACKNOWLEDGMENTS

We thank the anonymous referee that provided comments and suggestions that significantly improved the manuscript. Joseph Cassinelli inspired this work with helpful conversations and notes. We thank Bart Wakker for help with the data reduction.

Support for program 13239 was provided by NASA through a grant from the Space Telescope Science Institute, which is operated by the Association of Universities for Research in Astronomy, Inc., under NASA contract NAS 5-26555. All of the data presented in this paper were obtained from the Mikulski Archive for Space Telescopes (MAST). STScI is operated by the Association of Universities for Research in Astronomy, Inc., under NASA contract NAS 5-26555. Support for MAST for non-HST data is provided by the NASA Office of Space Science via grant NNX09AF08G and by other grants and contracts.

## REFERENCES

- Alexandroff R. M., Heckman T. M., Borthakur S., Overzier R., Leitherer C., 2015, *ApJ*, **810**, 104
- Asplund M., Grevesse N., Sauval A. J., Scott P., 2009, *ARA&A*, **47**, 481
- Baldwin J. A., Ferland G. J., Martin P. G., Corbin M. R., Cota S. A., Peterson B. M., Slettebak A., 1991, *ApJ*, **374**, 580
- Benson A. J., Bower R. G., Frenk C. S., Lacey C. G., Baugh C. M., Cole S., 2003, *ApJ*, **599**, 38
- Bordoloi R., Rigby J. R., Tumlinson J., Bayliss M. B., Sharon K., Gladders M. G., Wuyts E., 2016, *MNRAS*, **458**, 1891
- Brüggen M., Scannapieco E., 2016, preprint, ([arXiv:1602.01843](https://arxiv.org/abs/1602.01843))
- Buat V., Giovannoli E., Takeuchi T. T., Heinis S., Yuan F.-T., Burgarella D., Noll S., Iglesias-Páramo J., 2011, *A&A*, **529**, A22
- Bustard C., Zweibel E. G., D’Onghia E., 2016, *ApJ*, **819**, 29
- Calzetti D., Armus L., Bohlin R. C., Kinney A. L., Koornneef J., Storchi-Bergmann T., 2000, *ApJ*, **533**, 682
- Chabrier G., 2003, *PASP*, **115**, 763
- Chevalier R. A., Clegg A. W., 1985, *Nature*, **317**, 44
- Chisholm J., Tremonti C. A., Leitherer C., Chen Y., Wofford A., Lundgren B., 2015, *ApJ*, **811**, 149
- Chisholm J., Tremonti C. A., Leitherer C., Chen Y., Wofford A., 2016a, *MNRAS*, **457**, 3133
- Chisholm J., Tremonti Christy A., Leitherer C., Chen Y., 2016b, *MNRAS*, **463**, 541
- Cooper J. L., Bicknell G. V., Sutherland R. S., Bland-Hawthorn J., 2008, *ApJ*, **674**, 157
- Cooper J. L., Bicknell G. V., Sutherland R. S., Bland-Hawthorn J., 2009, *ApJ*, **703**, 330
- Dekel A., Silk J., 1986, *ApJ*, **303**, 39
- Dutton A. A., 2012, *MNRAS*, **424**, 3123
- Duval F., et al., 2016, *A&A*, **587**, A77
- Efstathiou G., 2000, *MNRAS*, **317**, 697
- Erb D. K., 2015, *Nature*, **523**, 169
- Ferland G. J., et al., 2013, *rmxaa*, **49**, 137
- Fox A. J., Richter P., Wakker B. P., Lehner N., Howk J. C., Ben Bekhti N., Bland-Hawthorn J., Lucas S., 2013, *ApJ*, **772**, 110
- Fox A. J., et al., 2014, *ApJ*, **787**, 147
- France K., Nell N., Green J. C., Leitherer C., 2010, *ApJ*, **722**, L80
- Green J. C., et al., 2012, *ApJ*, **744**, 60
- Hamann F., Barlow T. A., Junkkarinen V., Burbidge E. M., 1997, *ApJ*, **478**, 80
- Hayes M., et al., 2014, *ApJ*, **782**, 6
- Heckman T. M., Armus L., Miley G. K., 1990, *ApJS*, **74**, 833
- Heckman T. M., Lehnert M. D., Strickland D. K., Armus L., 2000, *ApJS*, **129**, 493
- Heckman T. M., Alexandroff R. M., Borthakur S., Overzier R., Leitherer C., 2015, *ApJ*, **809**, 147
- Hopkins P. F., Quataert E., Murray N., 2012, *MNRAS*, **421**, 3522

- Hopkins P. F., Kereš D., Oñorbe J., Faucher-Giguère C.-A., Quataert E., Murray N., Bullock J. S., 2014, *MNRAS*, **445**, 581
- James B. L., Aloisi A., Heckman T., Sohn S. T., Wolfe M. A., 2014, *ApJ*, **795**, 109
- Jarrett T. H., et al., 2013, *AJ*, **145**, 6
- Katz N., 1992, *ApJ*, **391**, 502
- Katz N., Weinberg D. H., Hernquist L., 1996, *ApJS*, **105**, 19
- Kereš D., Katz N., Davé R., Fardal M., Weinberg D. H., 2009, *MNRAS*, **396**, 2332
- Kim C.-G., Ostriker E. C., 2015, *ApJ*, **802**, 99
- Kim C.-G., Ostriker E. C., Raileanu R., 2017, *ApJ*, **834**, 25
- Klein R. I., McKee C. F., Colella P., 1994, *ApJ*, **420**, 213
- Lamers H. J. G. L. M., Cassinelli J. P., 1999, *Introduction to Stellar Winds*. Cambridge, UK: Cambridge University Press
- Leitherer C., et al., 1999, *ApJS*, **123**, 3
- Leitherer C., Ortiz Otálvaro P. A., Bresolin F., Kudritzki R.-P., Lo Faro B., Pauldrach A. W. A., Pettini M., Rix S. A., 2010, *ApJS*, **189**, 309
- Leitherer C., Chandar R., Tremonti C. A., Wofford A., Schaerer D., 2013, *ApJ*, **772**, 120
- Leroy A. K., et al., 2015, *ApJ*, **814**, 83
- Lopez L. A., Krumholz M. R., Bolatto A. D., Prochaska J. X., Ramirez-Ruiz E., 2011, *ApJ*, **731**, 91
- Lopez L. A., Krumholz M. R., Bolatto A. D., Prochaska J. X., Ramirez-Ruiz E., Castro D., 2014, *ApJ*, **795**, 121
- Mac Low M.-M., McCray R., Norman M. L., 1989, *ApJ*, **337**, 141
- Markwardt C. B., 2009, in Bohlender D. A., Durand D., Dowler P., eds, *Astronomical Society of the Pacific Conference Series* Vol. 411, *Astronomical Data Analysis Software and Systems XVIII*. p. 251 ([arXiv:0902.2850](https://arxiv.org/abs/0902.2850))
- Martin C. L., 2005, *ApJ*, **621**, 227
- Martin C. L., Bouché N., 2009, *ApJ*, **703**, 1394
- Martin D. C., et al., 2005, *ApJ*, **619**, L1
- Mateo M. L., 1998, *ARA&A*, **36**, 435
- McKee C. F., Ostriker J. P., 1977, *ApJ*, **218**, 148
- Meynet G., Maeder A., Schaller G., Schaerer D., Charbonnel C., 1994, *A&AS*, **103**, 97
- Moster B. P., Somerville R. S., Maulbetsch C., van den Bosch F. C., Macciò A. V., Naab T., Oser L., 2010, *ApJ*, **710**, 903
- Muratov A. L., Kereš D., Faucher-Giguère C.-A., Hopkins P. F., Quataert E., Murray N., 2015, *MNRAS*, **454**, 2691
- Murray N., Quataert E., Thompson T. A., 2005, *ApJ*, **618**, 569
- Murray N., Martin C. L., Quataert E., Thompson T. A., 2007, *ApJ*, **660**, 211
- Navarro J. F., White S. D. M., 1993, *MNRAS*, **265**, 271
- Oppenheimer B. D., Davé R., 2006, *MNRAS*, **373**, 1265
- Oppenheimer B. D., Davé R., 2008, *MNRAS*, **387**, 577
- Östlin G., et al., 2014, *ApJ*, **797**, 11
- Pardy S. A., et al., 2014, *ApJ*, **794**, 101
- Prochaska J. X., Kasen D., Rubin K., 2011, *ApJ*, **734**, 24
- Querejeta M., et al., 2015, *ApJS*, **219**, 5
- Reyes R., Mandelbaum R., Gunn J. E., Pizagno J., Lackner C. N., 2011, *MNRAS*, **417**, 2347
- Richter P., Fox A. J., Wakker B. P., Lehner N., Howk J. C., Bland-Hawthorn J., Ben Bekhti N., Fechner C., 2013, *ApJ*, **772**, 111
- Rivera-Thorsen T. E., et al., 2015, *ApJ*, **805**, 14
- Rosdahl J., Schaye J., Dubois Y., Kimm T., Teyssier R., 2016, preprint, ([arXiv:1609.01296](https://arxiv.org/abs/1609.01296))
- Rubin K. H. R., Prochaska J. X., Koo D. C., Phillips A. C., Martin C. L., Winstrom L. O., 2014, *ApJ*, **794**, 156
- Rupke D. S., Veilleux S., Sanders D. B., 2005, *ApJS*, **160**, 87
- Scannapieco E., Brüggem M., 2015, *ApJ*, **805**, 158
- Scarlata C., Panagia N., 2015, *ApJ*, **801**, 43
- Schaye J., et al., 2015, *MNRAS*, **446**, 521
- Shapiro P. R., Field G. B., 1976, *ApJ*, **205**, 762
- Shopbell P. L., Bland-Hawthorn J., 1998, *ApJ*, **493**, 129
- Sobolev V. V., 1960, *Moving envelopes of stars*. "Cambridge: Harvard University Press"
- Somerville R. S., Davé R., 2015, *ARA&A*, **53**, 51
- Somerville R. S., Hopkins P. F., Cox T. J., Robertson B. E., Hernquist L., 2008, *MNRAS*, **391**, 481
- Springel V., Hernquist L., 2003, *MNRAS*, **339**, 312
- Steidel C. C., Erb D. K., Shapley A. E., Pettini M., Reddy N., Bogosavljević M., Rudie G. C., Rakic O., 2010, *ApJ*, **717**, 289
- Strickland D. K., Heckman T. M., 2009, *ApJ*, **697**, 2030
- Thompson T. A., Quataert E., Zhang D., Weinberg D. H., 2016, *MNRAS*, **455**, 1830
- Thornton K., Gaudlitz M., Janka H.-T., Steinmetz M., 1998, *ApJ*, **500**, 95
- Tumlinson J., et al., 2011, *Science*, **334**, 948
- Veilleux S., Cecil G., Bland-Hawthorn J., 2005, *ARA&A*, **43**, 769
- Vogelsberger M., Genel S., Sijacki D., Torrey P., Springel V., Hernquist L., 2013, *MNRAS*, **436**, 3031
- Vogelsberger M., et al., 2014, *MNRAS*, **444**, 1518
- Wakker B. P., Hernandez A. K., French D. M., Kim T.-S., Oppenheimer B. D., Savage B. D., 2015, *ApJ*, **814**, 40
- Weaver R., McCray R., Castor J., Shapiro P., Moore R., 1977, *ApJ*, **218**, 377
- Weiner B. J., et al., 2009, *ApJ*, **692**, 187
- Werk J. K., Prochaska J. X., Thom C., Tumlinson J., Tripp T. M., O'Meara J. M., Peeples M. S., 2013, *ApJS*, **204**, 17
- Werk J. K., et al., 2014, *ApJ*, **792**, 8
- White S. D. M., Frenk C. S., 1991, *ApJ*, **379**, 52
- Wofford A., Leitherer C., Salzer J., 2013, *ApJ*, **765**, 118
- Wright E. L., et al., 2010, *AJ*, **140**, 1868

This paper has been typeset from a  $\text{\TeX}/\text{\LaTeX}$  file prepared by the author.

## APPENDIX A: OPTICAL DEPTH AND COVERING FRACTION PLOTS

Here we include the plots of the velocity-resolved  $\tau$  (upper panels) and  $C_f$  (lower panels) for the entire sample. Fits to the lines, using Equation 6 are shown by the solid line. The velocity resolution is marked in the upper portion of each panel.

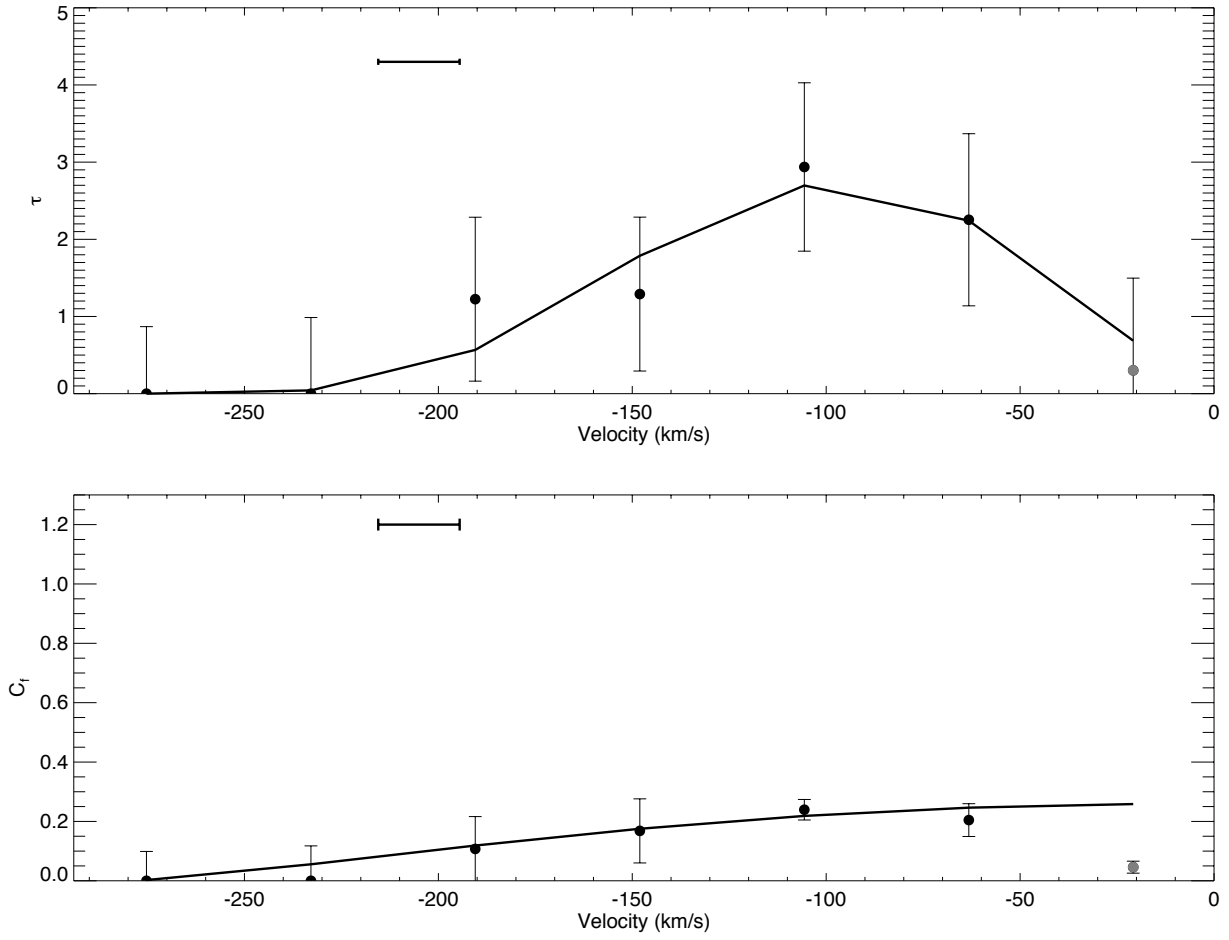


**Figure A1.** The velocity resolved Si IV optical depth ( $\tau$ ; upper panel) and covering fraction ( $C_f$ ; lower panel) for SBS1415+437, as derived from Equation 2. The  $\tau$  is fit (solid line) assuming a Sobolev optical depth, and the  $C_f$  is fit assuming a radial power-law  $C_f$ , as given by Equation 6. Gray points are excluded from the fit due to contamination of resonance emission. The spectral resolution is given as a bar in the upper portion of each panel.



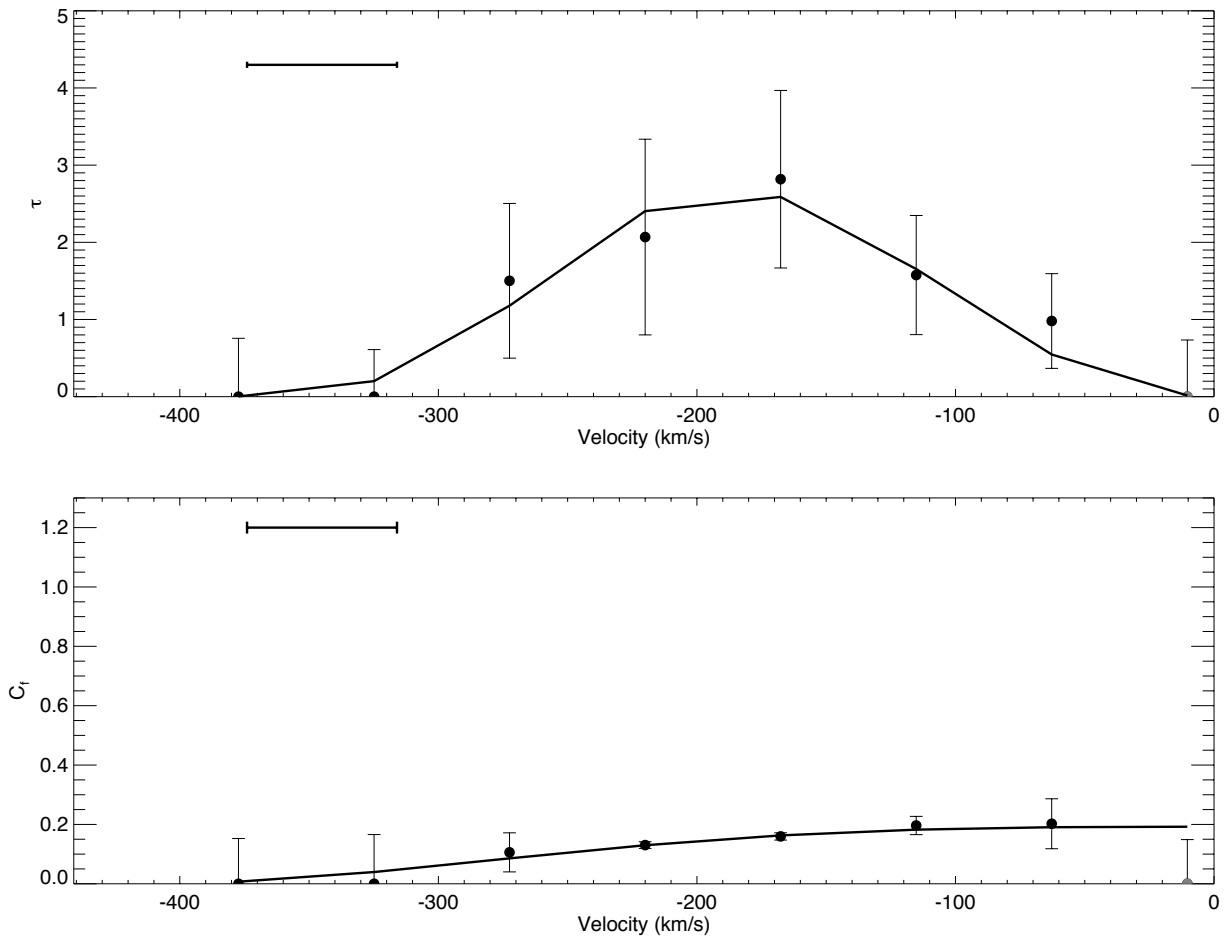
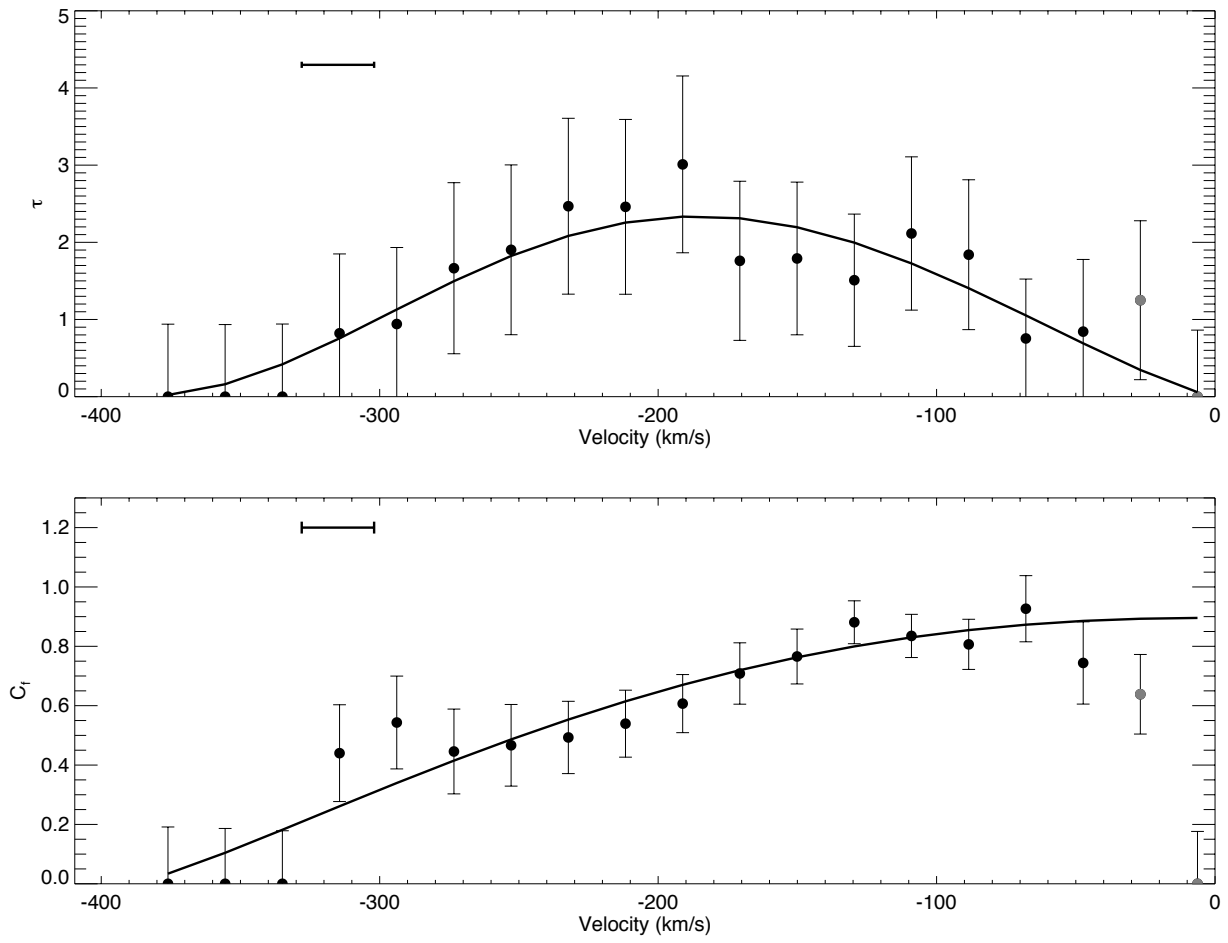


Figure A2. Same as Figure A1 but for 1 Zw 18. .



**Figure A3.** Same as [Figure A1](#) but for MRK 1486.

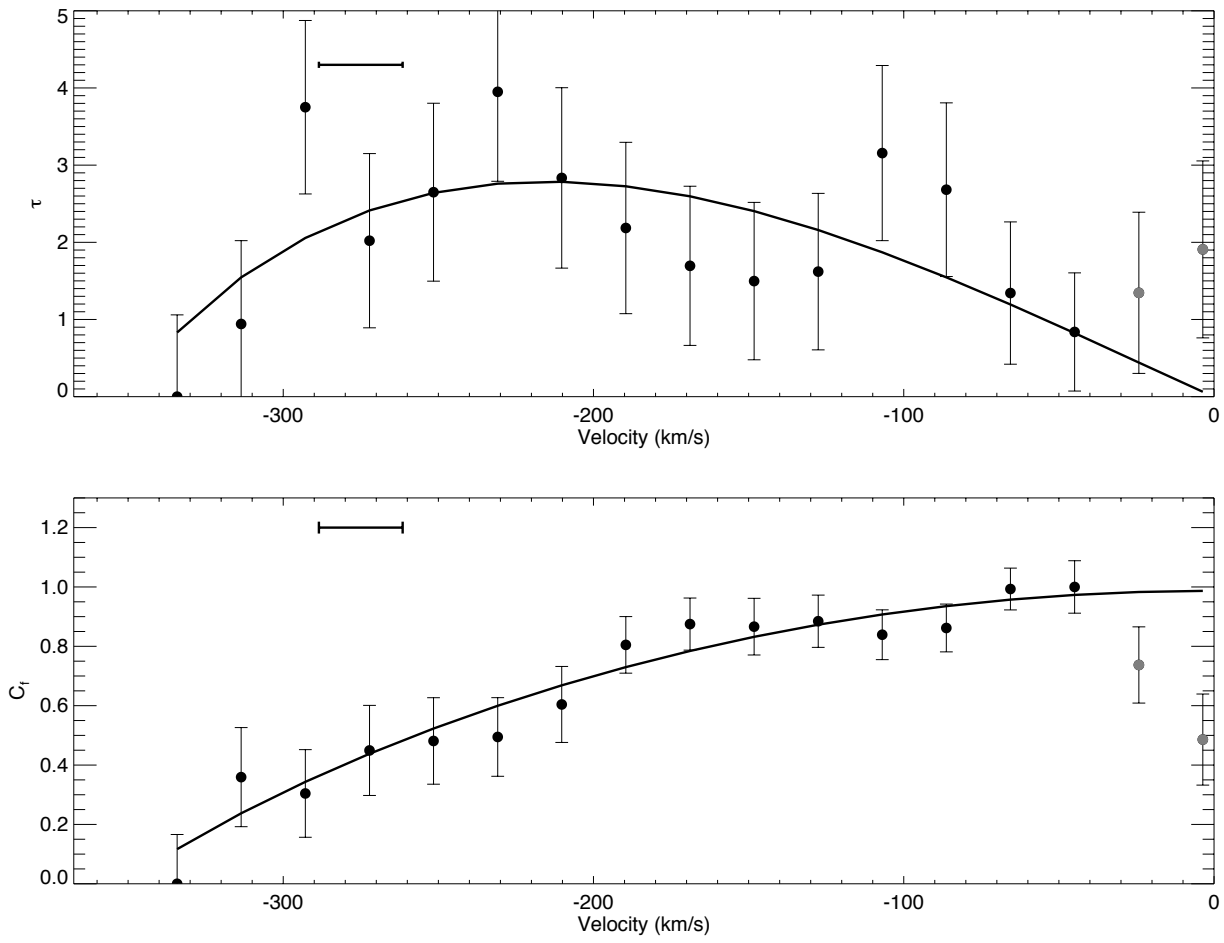
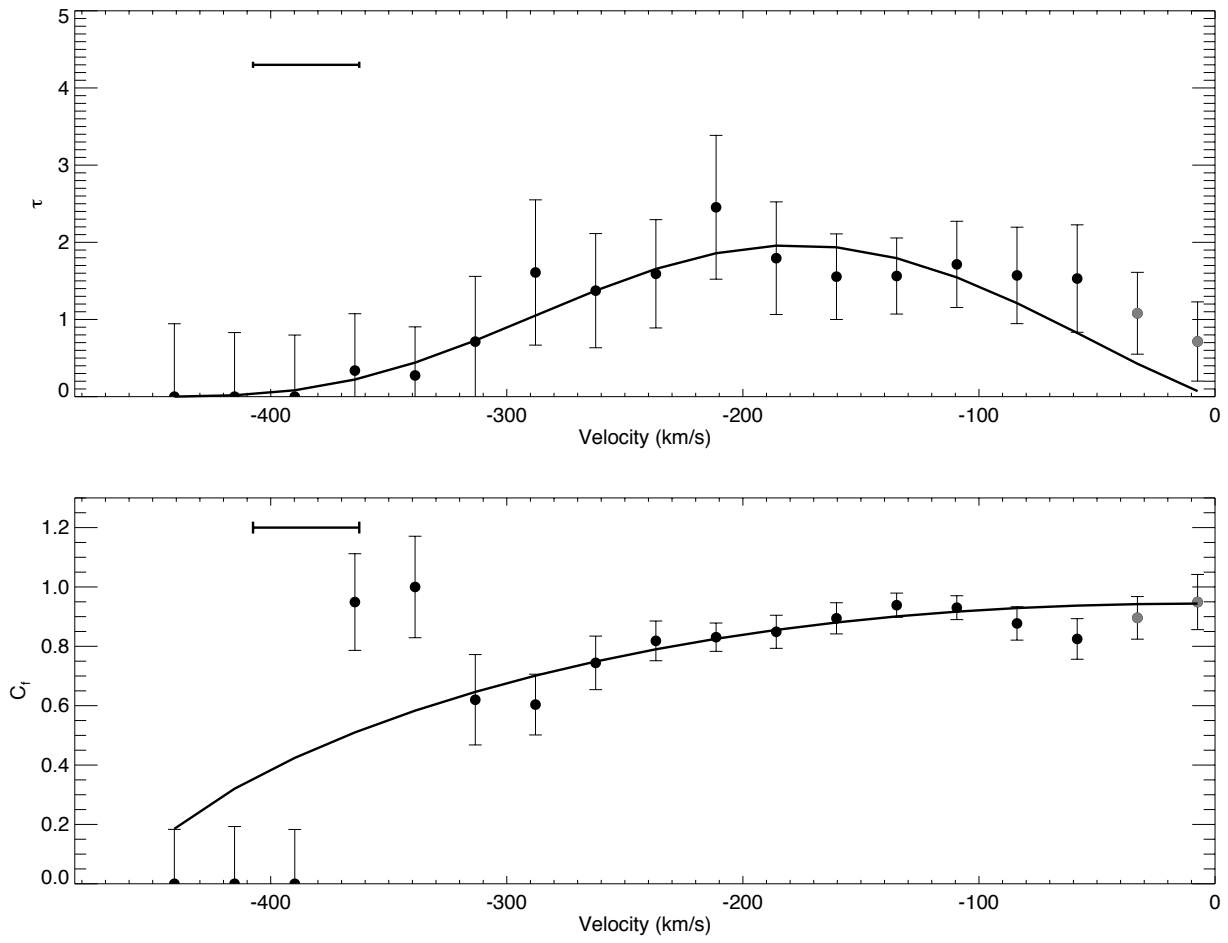


Figure A4. Same as Figure A1 but for KISSR 1578.



**Figure A5.** Same as [Figure A1](#) but for Haro 11.



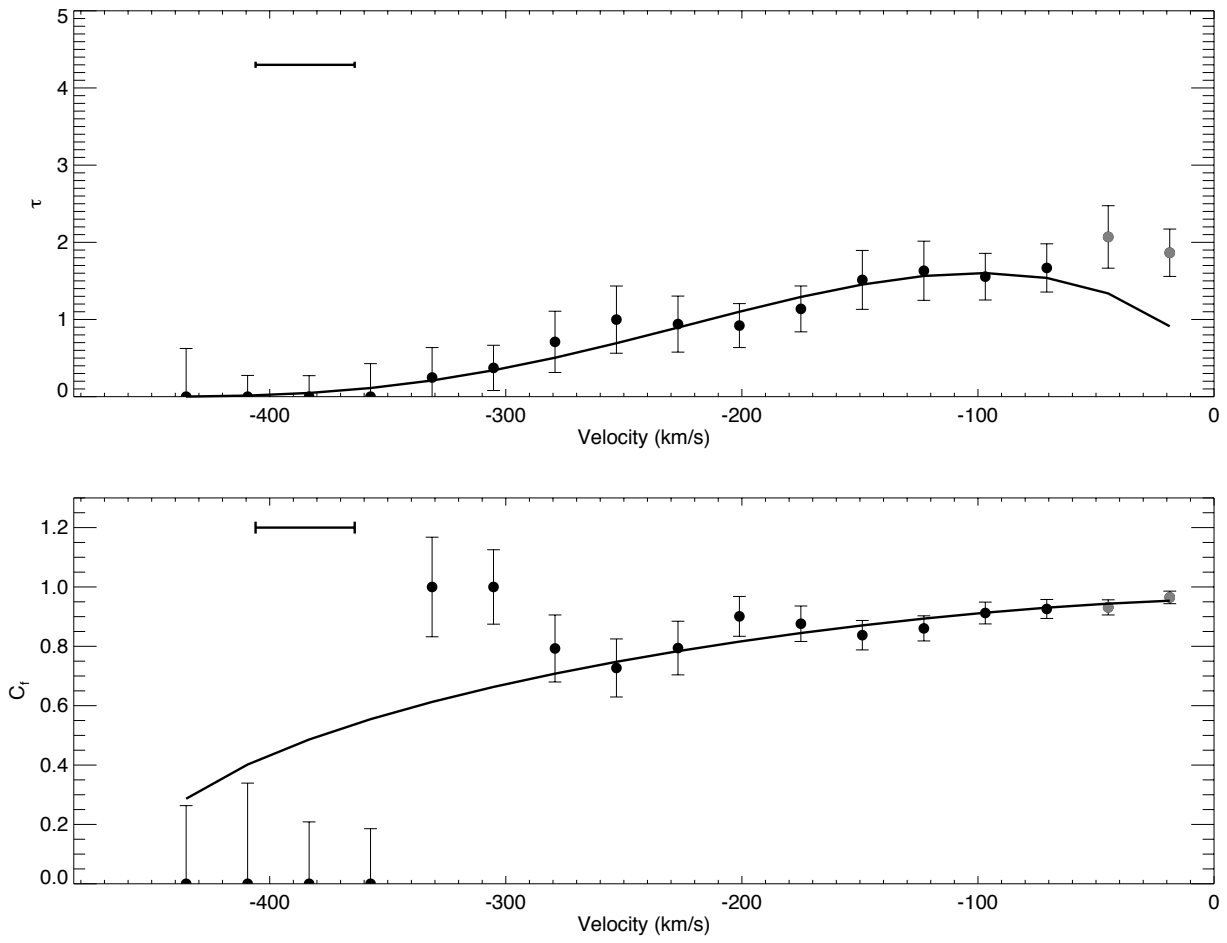
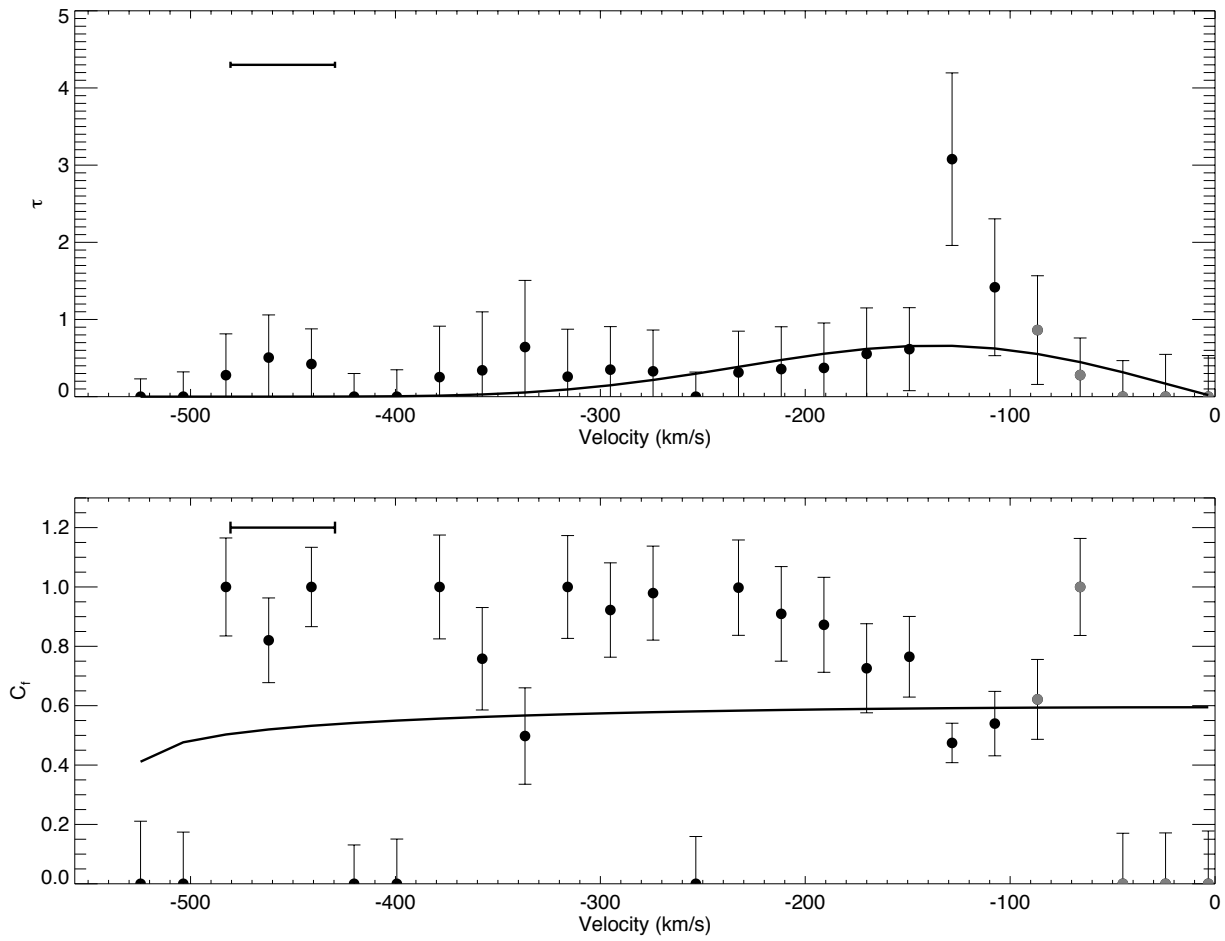


Figure A6. Same as Figure A1 but for NGC 7714.



**Figure A7.** Same as [Figure A1](#) but for IRAS08449+6517. This galaxy is not included in the analysis because the line profile cannot match the proposed model of § 2.3

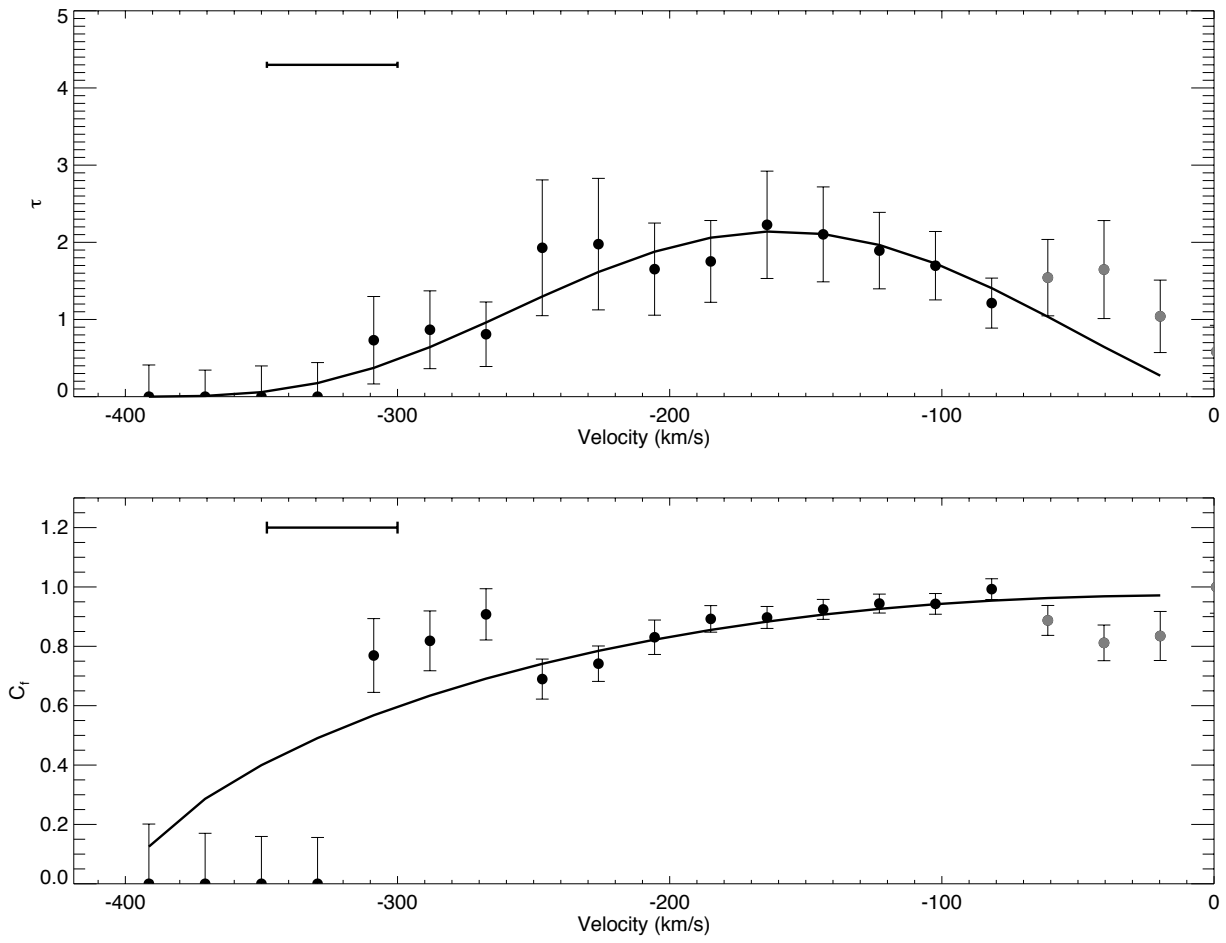


Figure A8. Same as Figure A1 but for NGC 6090.